



HAL
open science

Influence of boundary conditions on computation of the effective thermal conductivity of foams

Zi Kang Low, N Blal, N Naouar, D Baillis

► **To cite this version:**

Zi Kang Low, N Blal, N Naouar, D Baillis. Influence of boundary conditions on computation of the effective thermal conductivity of foams. *International Journal of Heat and Mass Transfer*, 2020, 10.1016/j.ijheatmasstransfer.2020.119781 . hal-03019642

HAL Id: hal-03019642

<https://hal.science/hal-03019642v1>

Submitted on 9 Dec 2020

HAL is a multi-disciplinary open access archive for the deposit and dissemination of scientific research documents, whether they are published or not. The documents may come from teaching and research institutions in France or abroad, or from public or private research centers.

L'archive ouverte pluridisciplinaire **HAL**, est destinée au dépôt et à la diffusion de documents scientifiques de niveau recherche, publiés ou non, émanant des établissements d'enseignement et de recherche français ou étrangers, des laboratoires publics ou privés.

Influence of boundary conditions on computation of the effective thermal conductivity of foams

Z.K. Low^{a,b,*}, N. Blal^a, N. Naouar^a, D. Baillis^a

^aUniv Lyon, INSA-Lyon, CNRS UMR5259, LaMCoS, F-69621 Villeurbanne, France.

^bSaint-Gobain Research Provence, F-84306 Cavaillon, France.

Abstract

Accurate numerical simulation of the effective thermal conductivity (ETC) of 3D pore-scale foam models requires a judicious choice of boundary conditions, as the computational domains are often smaller than the representative volume element, giving rise to considerable edge effects. Within the finite element homogenization framework, a set of mixed boundary conditions are considered alongside the usual uniform and periodic boundary conditions. Validity criteria and order relations, demonstrated from entropy-based principles, are numerically verified on unit cell-based geometries, random virtual periodic foams, and non-periodic tomography-reconstructed foams of equivalent microstructure. A statistical treatment based on the integral range provides confidence intervals for the estimated ETC. For foam samples with random homogeneous porosity, the mixed boundary conditions are shown to fulfill the macrohomogeneity condition and thus provide thermodynamically valid ETC estimates. For periodic foams with irregular microstructure, the ETC is very slightly underestimated under the mixed boundary conditions. For non-periodic geometries, it is shown that periodic boundary conditions—commonly viewed as the reference—underestimate the ETC due to boundary geometry mismatch, while the mixed boundary conditions give a more accurate and precise estimate.

Keywords: Foam, Thermal conductivity, Homogenization, Boundary conditions, Finite elements

1. Introduction

Cellular foam materials are a source of interest in many fields [1–3] as they combine attractive thermal properties with good strength-to-weight ratio [4]. Accurate modeling of the foam effective thermal conductivity (ETC) is important on account of the difficulties in performing precise measurements under service conditions (e.g., refractory ceramic foams with service temperatures up to 1700 °C [5]). While analytical relations between the ETC and microstructural parameters are abundant in the literature [6, 7], most still require calibration or validation against empirical data [7] before they may be applied to particular classes of materials. As such, many recent studies have focused on 3D pore-scale numerical simulations on either regular unit cell geometries [8],

*Corresponding author

Email address: zi.low@insa-lyon.fr (Z.K. Low)

Nomenclature

Scalars are written in *regular italic* font, while first- and second-order tensors are denoted with *bold face italics*.

Latin

ℓ	Micro-scale characteristic length
P	Probability
\mathbb{R}^3	Cartesian frame
S	Entropy functional
A	Area
C	Covariance
e	Basis vector
F	Macroscopic heat flux
f	Volume fraction
G	Macroscopic temperature gradient
h	Distance
I	Identity
J	Integral range
j	Direction index
k	Thermal conductivity
L	Length
N	Number
n	Normal direction
Q	Heat flow
q	Heat flux
R	Rotation
r	Residual
T	Absolute temperature
V	Volume
x	Position

Greek

Δ	Difference
ϵ	Precision, error
μ	Mean
Ω	Domain
σ	Variance

θ	Relative temperature
----------	----------------------

Superscripts and Subscripts

+/-	Opposite sides on the boundary
0	Reference, Arbitrary, Constant
adm	Admissible
app	Apparent
eff	Effective
sol	Solution
c	Complementary
D	Diagonal
p	Pore
s	Solid

Operators and accents

∇	Del operator
\cdot	Dot product, single tensor contraction
∂X	Boundary of X
$\langle X \rangle$	Volume average of X
$[X]$	Matrix representation
\bar{X}	Imposed values of X
\tilde{X}	Fluctuating component of X

Acronyms

ATC	Apparent thermal conductivity
ETC	Effective thermal conductivity
MBC	Mixed boundary conditions
PBC	Periodic boundary conditions
PSD	Pore size distribution
RVE	Representative volume element
SSA	Specific surface area
UHF	Uniform heat flux
UTG	Uniform temperature gradient

digitally generated random periodic foams [9–11], or tomography-reconstructed real foam models [1, 2, 12–15].

Finite element-based computational homogenization [16–19] has been used to accurately predict the ETC tensor of heterogeneous materials such as composites [11] and porous media [20, 21] from microstructural descriptions of the material. In this scheme, the ETC is classically obtained by resolving uniform heat flux (UHF) and uniform temperature gradient (UTG) boundary value problems [22] on computational domains of increasing size, until the resulting apparent thermal conductivities (ATC) converge to the same value: the ETC. The domain at which convergence is reached is then defined as a representative volume element (RVE). By this definition, the ETC satisfies the macrohomogeneity condition¹, i.e., fundamental thermodynamic quantities (entropy in the case of heat conduction) are conserved during scale transition [23]. However, real porous media such as foams can have prohibitively large RVE sizes due to the random microstructure and

¹The analogous condition in the mechanical case is commonly called Hill's lemma or the Hill-Mandel condition, and is based on conservation of the mechanical strain energy during scale transitions.

high contrast in phase properties [20, 21, 24]. Therefore, it is often necessary to estimate the ETC using computational domains smaller than the RVE (for example, with statistical treatments based on the integral range [20]). Contrary to the ETC which is intrinsic to the material, the ATC of such domains may be highly sensitive to boundary conditions due to edge effects, even when convective and radiative heat transfer are neglected [20, 24].

With their roots in the pioneering works on asymptotic homogenization [25–27], periodic boundary conditions (PBC)² have been shown to satisfy the macrohomogeneity condition, and to directly yield the ETC when applied to single periodic unit cells [17, 24]. Even though the PBC implicitly assume a periodic computational geometry, they have also been applied in numerous instances to non-periodic geometries such as tomography-reconstructed microstructures [14, 15, 20, 21, 30]. The commonly held view is that the PBC provide the best possible ETC estimate even for non-periodic geometries [16, 19], and that the error due to geometrical non-periodicity [30] would vanish if the computational domain is sufficiently large [29]. However, no evidence has been found to support this view in the case of highly porous real foam models obtained by tomographic reconstruction, which are often smaller than the RVE.

Much past work involving numerical modeling on tomography-reconstructed foams (e.g., [1, 2, 13, 31]) used instead a set of mixed boundary conditions (MBC) that simulates steady-state experimental configurations such as the guarded hot plate method [32]. With a parallelepipedic domain of the sample material, uniform temperatures are fixed on two plane-parallel faces with a small temperature difference $\Delta\theta$ between them, while adiabatic conditions are applied to the four other faces. If the macroscopic material behavior is isotropic or orthotropic [2, 31], a unidirectional heat flow Q exists within the sample, and a scalar apparent conductivity k_{1D} is computed:

$$k_{1D} = -\left(\frac{Q}{A}\right)\left(\frac{\Delta L}{\Delta\theta}\right) \quad (1)$$

with A being the surface area of the hot and cold faces, and ΔL being the distance between them. Despite their widespread use by the porous media community (e.g., [1, 2, 13, 31]), to the present authors' knowledge, these MBC have only been sporadically used within the computational homogenization framework [21, 24]. This is likely due to the uncertainty on whether the resulting ATC satisfies the macrohomogeneity condition, especially for anisotropic microstructures. The accuracy and precision of the MBC results relative to those given by the uniform and periodic boundary conditions are also unclear, save for a few specific cases: Jiang et al. [24] found that the MBC and PBC gave equally accurate results for 2D isotropic unit cells, and Dirrenberger et al. [21] found that for stochastic fibrous samples, larger sample volumes were required to achieve the same precision with the MBC than with the UTG. For foam geometries smaller than the RVE, these questions remain open.

Through theoretical demonstrations verified with numerical results, the present work investigates the validity, accuracy, and precision of the ETC of foams estimated via computational homogenization under uniform, periodic and mixed boundary conditions. The aim is to clarify the

²Periodic boundary conditions are also used in the volume averaging scheme [28], which gives the same result as asymptotic homogenization under equivalent assumptions despite being theoretically distinct [29].

most appropriate boundary conditions for different types of 3D foam models (unit cell-based geometries, virtual periodic foams, and tomography-reconstructed real foams), so as to pave the way for more accurate predictions of microstructure-property relations. Section 2 describes the characterization of tomography-reconstructed real foams through image analysis and the generation of periodic foams of equivalent microstructure. Section 3 formalizes the homogenization problem and theoretically demonstrates validity criteria and order relations for the different ATC using entropy-based principles. Section 4 presents the computational strategy, clarifies the concepts of validity, accuracy, and precision of the ETC estimates, and describes the statistical treatment used to account for the stochastic real foam microstructure. Results for the different numerical case studies are then discussed in section 5.

1.1. Mathematical notation

Tensorial notation is used in the equations, with scalars in *regular italic* font, and first- and second-order tensors denoted with ***bold face italics***. Tensors expressed as vectors or matrices (denoted with square brackets $[\bullet]$) are given with respect to the Cartesian reference frame $\{\mathbf{e}_1, \mathbf{e}_2, \mathbf{e}_3\}$, unless otherwise specified.

2. Characterization and modeling of foam morphology

This section describes the characterization and modeling of the different types of foams studied in this work. Two types of random foam models are considered: tomography-reconstructed samples of a reference ceramic foam which provide the most realistic description of the pore scale morphology, and digitally generated periodic foams of equivalent microstructure. In addition, non-periodic regular structures were also created from an orthotropic unit cell for a preliminary study (described further in subsection 5.1).

2.1. 3D imaging and reconstruction of real foam samples

The reference material for this study is NorFoam XPure® by Saint-Gobain, a high-purity alumina foam for high temperature thermal insulation [5]. X-ray micro-computed tomography of the reference material was performed using the *Phoenix v|tome|x s* by GE. A cubic volume of 92.04 mm^3 was scanned and stored as a grayscale image stack. Automatic thresholding and denoising were performed using the Fiji software [33] (see Figures 1(a) to (c)) to obtain a binary image stack containing $516 \times 516 \times 516$ voxels with a voxel size of $8.75 \mu\text{m}$). The porosity of the reconstructed real foam is $74 \pm 2\%$, which agrees well with the measured apparent density of the physical samples (the uncertainty reflects the sensitivity towards the image processing parameters).

2.2. Quantitative analysis of microstructural parameters

Pore size distribution. The reference alumina foam has a predominantly open-cell foam structure with interconnected spheroidal pores. The principal microstructural parameter is taken as the pore size distribution (PSD), with pore size defined as the diameter of an equal-volume sphere. Segmentation of the pore phase is performed with a watershed algorithm based on a maximal ball approach implemented in the iMorph software [34]. In Figure 2(a), the PSD based on pore count (with the diameter in μm) is shown to follow a lognormal distribution of parameters $\mu = 4.5$ and

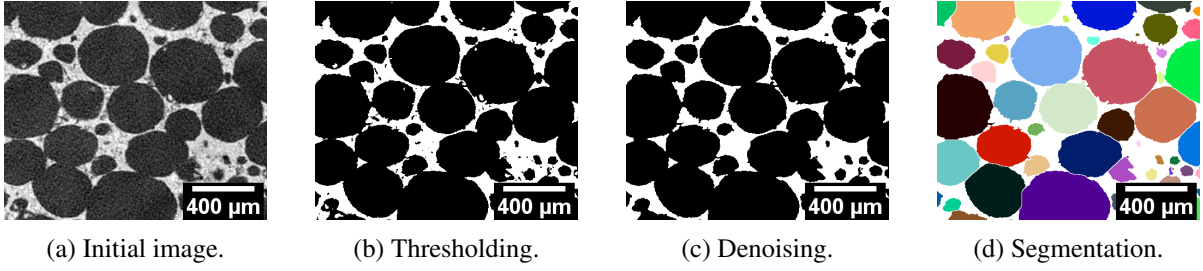


Figure 1: Image processing steps.

$\sigma = 0.97$ representing the mean and standard deviation of the diameter's logarithm respectively. The median diameter is $140 \mu\text{m}$ based on pore count, and $590 \mu\text{m}$ based on pore volume.

Pore connectivity. Once segmentation of the pore phase is performed, the pore network can be obtained by connecting the barycenter of each pore to those of its closest neighbors. The pore connectivity is then described by the mean number of neighboring pores in contact with any given pore, i.e., those having at least 1 voxel in common. This parameter is often considered in relation to heat and mass transport through the pore phase.

Specific surface area (SSA). The specific surface area is the total foam surface area per unit apparent volume, and represents the area available for heat exchange between the pore and solid phase. iMorph uses a marching cubes algorithm [34] to generate a surface mesh of the pore-solid interface constituted of triangular elements; the specific surface area is then estimated using the sum of the elements' areas.

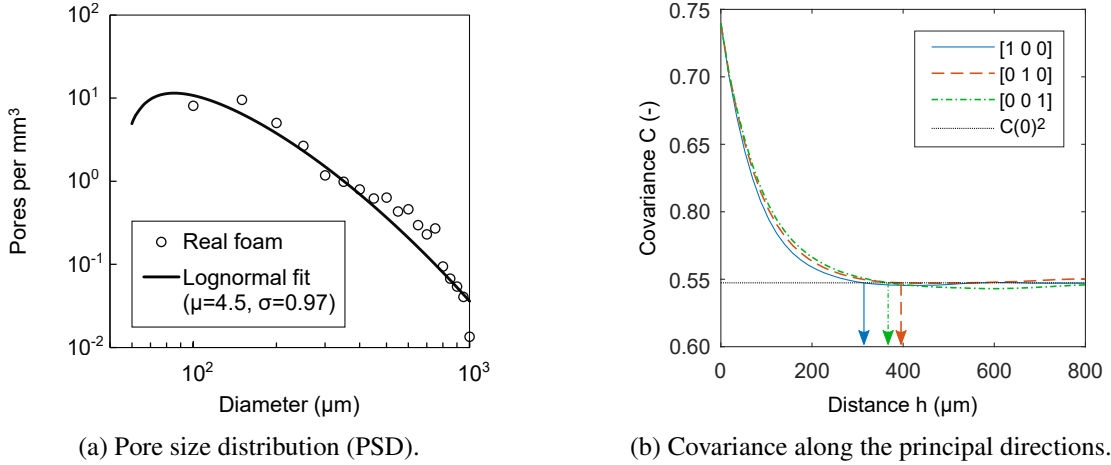


Figure 2: Microstructural characteristics of the real foam.

Covariance range. The morphological covariance characterizes the geometrical dispersion within the foam sample [20]. Let \mathbf{x} be a point in the sample. Denoting Ω_p the set of all points belonging to the pore phase and $\mathbf{h} \in \mathbb{R}^3$ an arbitrary distance vector, the morphological covariance $C(\mathbf{h})$ is

an even function describing the probability that both points \mathbf{x} and $\mathbf{x} + \mathbf{h}$ belong to the pore phase:

$$C(\mathbf{h}) = \mathbb{P}(\{\mathbf{x} \in \Omega_p\} \cap \{\mathbf{x} + \mathbf{h} \in \Omega_p\}) = C(-\mathbf{h}) \quad (2)$$

When $\mathbf{h} = \mathbf{0}$, the covariance is simply equal to the porosity f_p . As $|\mathbf{h}| \rightarrow \infty$, $C(\mathbf{h})$ tends to the theoretical asymptotic value f_p^2 (two points infinitely far apart are uncorrelated). In most cases, there exists a finite distance called the covariance range at which this asymptotic value is reached. The covariance range depends on the size and arrangement of pores, and thus represents the characteristic length ℓ of the micro-scale in a given direction [20]. Points at distances larger than this range are considered statistically independent in terms of their microstructure. In Figure 2(b), the covariance ranges along the principal directions of the cubic geometry vary from 333 μm to 373 μm , which is approximately 3 times the median pore diameter of 140 μm . The tiny variation along the different principal directions suggests a very slight anisotropy in the material.

2.3. Generation of equivalent periodic foam models

Recent studies on pore-scale foam modeling have increasingly favored the use of digitally generated random polydisperse foam models over traditional unit cell descriptions [35], with Voronoi-based tessellations often used to simulate the distinctively skeletal structure of ultra-low density foams (usually having porosities of over 90%) [4, 9, 10, 36]. However, for ceramic foams of slightly lower porosity (approximately between 60% and 85%) fabricated by direct foaming of a ceramic slurry, spheroidal pores tend to be observed instead [37], as is the case with NorFoam XPure®. For this class of foams, the foam structure is more closely simulated as a solid matrix with packed spherical inclusions [10, 38]. The method of Cunsolo et al. [10] chosen to generate the virtual foams in this work will be briefly described in this subsection.

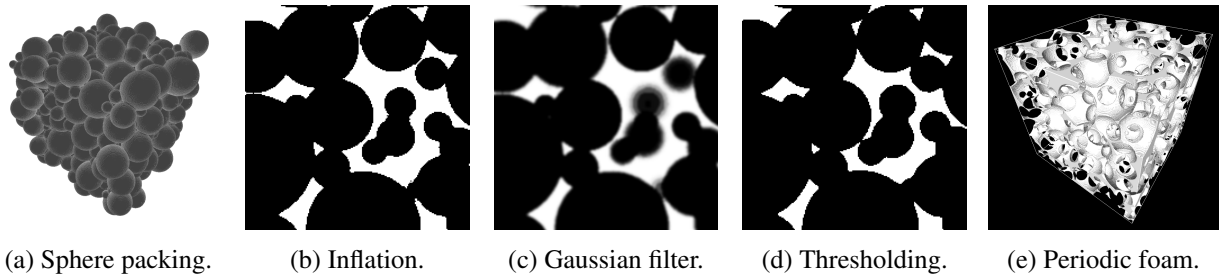


Figure 3: Generation of periodic foam models with the algorithm of Cunsolo et al. [10].

Four microstructural parameters are given as input: the target porosity f_p , the standard deviation σ of the diameter's logarithm, the edge length L of the cubic domain, and the number of pores in the domain. Figure 3 summarizes the foam generation workflow. The process starts with the generation of a random periodic packing of non-overlapping spheres, with relative diameters following a normalized lognormal PSD of parameter σ . The spheres are first inflated with their relative size unchanged, allowing intersections, to roughly match the target porosity. The structure is then converted into binary voxel format. A Gaussian blur filter followed by grayscale thresholding allows fine-tuning of the porosity while softening sharp edges in the foam structure, giving

Foam type & volume (mm ³)	PSD: Pores per mm ³ vs. diameter (μm)	Pore connectivity	SSA (mm ⁻¹)	Covariance range (μm)
Real foam ○ ($V = 92.04$)		3.93	10.7	353 ± 20
Virtual foam Δ ($V = 2.74$)		3.5 ± 0.7	9.7 ± 0.5	429 ± 184
Virtual foam □ ($V = 11.78$)		3.9 ± 0.4	8.4 ± 0.3	696 ± 345

Table 1: Comparison of key microstructural parameters between the real and virtual foams: pore size distribution (PSD), pore connectivity, specific surface area (SSA), and covariance range. For the virtual foams, the mean and standard deviations across 10 realizations are given.

results similar to more sophisticated but computationally demanding approaches (e.g., the discrete element approach of Dyck and Straatman [38]).

Virtual foams of 6 distinct volumes ranging from 2.74 mm³ to 11.78 mm³ with 10 realizations for each volume are generated. The target porosity of 74% is achieved within voxel precision for all virtual foams. The same microstructural analysis described in subsection 2.2 is then applied to the virtual foams, with the results for the smallest and largest foams summarized in Table 1. The PSD, connectivity and SSA of the virtual foams agree remarkably well with those of the real foam, especially given that the absolute pore sizes were not fixed during the generation procedure. The higher mean covariance range in the virtual foams with a wider scatter suggests a less random pore arrangement in the virtual foam resulting from the periodicity constraint, with a higher degree of geometrical anisotropy within certain realizations due to the presence of a few extremely large pores. As the covariance ranges remain smaller than the cubic edge length L , the separation of micro- and macro-scales is upheld, and the realizations are statistically independent of one another.

2.4. Creation of non-periodic unit cell-based structures

For the preliminary study described in subsection 5.1, regular geometries that possess the key characteristics of the tomography-reconstructed foams (non-periodicity, anisotropy, high porosity) are created according to the method described below.

A reference orthotropic unit cell is first built, starting from a motif comprised of a body-centered cubic arrangement of overlapping spheres (Figure 4(a)). An oblong $4 \times 2 \times 1$ tessellation of said motif is created (Figure 4(b)), then compressed into a cube, resulting in an orthotropic tessellation of overlapping ellipsoids. Finally, the inverse of this tessellation (Figure 4(c)) gives a periodic, orthotropic unit cell with interconnected ellipsoidal pores. The porosity of $f_p = 71.3\%$ is in the same range as the studied foams.

Non-periodic anisotropic geometries are then created as follows: a large 3D tessellation of the orthotropic unit cell is created, an arbitrary rotation is applied to the tessellation, then a cube is cut according to the initial Cartesian reference frame to give the final geometry. They are then used for the preliminary study described in subsection 5.1; notably, Table 2 contains examples of the anisotropic geometries obtained with the present method.

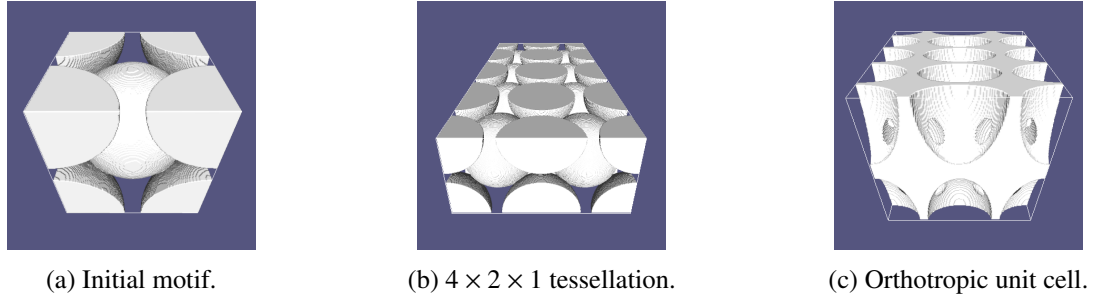


Figure 4: Generation of the orthotropic unit cell.

3. Theoretical study on boundary conditions

Heat transfer within engineering parts or structures made of foams typically occur over length scales much greater than the characteristic sizes of the foams' heterogeneities. Applying the principle of scale separation, two distinct scales can be considered. At the macro-scale, one is concerned with the thermal loading and response of the engineering structure, and the behavior of the foam may be represented by an effective thermal conductivity (ETC) tensor \mathbf{k}_{eff} . While a phenomenological model for \mathbf{k}_{eff} can be derived from experimental measurements, this approach is generally cumbersome. Computational homogenization provides a more versatile way to deduce \mathbf{k}_{eff} by simulating heat transfer at the micro-scale on explicit representations of the foam morphology (see Figure 5). The chosen micro-scale boundary conditions should satisfy the so-called "macrohomogeneity condition" to ensure fundamental thermodynamic quantities remain consistent during scale transition.

Four boundary conditions for the micro-scale problem are examined in this work: uniform heat flux (UHF), uniform temperature gradient (UTG), periodic (PBC) and mixed (MBC) boundary conditions. Assuming they satisfy the macrohomogeneity condition, these boundary conditions should predict the same macro-scale behavior when the computational geometry is large enough to be considered a representative volume element (RVE) of the foam. However, as most foam geometries are smaller than the RVE, different boundary conditions generally give different apparent thermal conductivity (ATC) tensors \mathbf{k}_{app} which are more or less accurate estimates of the ETC.

The governing equations of the two-scale problem are first provided in subsection 3.1. The different boundary conditions are then examined in subsection 3.2. In particular, validity criteria for the MBC are developed with respect to the macrohomogeneity condition. The maximum entropy principle is then used in subsection 3.3 to establish analytical order relations between the ATC computed under different boundary conditions.

3.1. Governing equations

3.1.1. Macro-scale problem

At the macro-scale, the foam may be approximated as an equivalent homogeneous medium with a second-order effective thermal conductivity (ETC) tensor \mathbf{k}_{eff} . In the absence of volumetric heat sources, steady-state heat transfer is described by the macro-scale Fourier's law:

$$\mathbf{F} = -\mathbf{k}_{\text{eff}} \cdot \mathbf{G} \quad \text{with} \quad \nabla \cdot \mathbf{F} = 0 \quad (3)$$

where \mathbf{F} and \mathbf{G} are the macroscopic heat flux and temperature gradient vectors respectively.

If \mathbf{k}_{eff} is known, the heat flux and temperature fields across the entire macroscopic domain can be computed for any well-posed loading case. One way to obtain \mathbf{k}_{eff} is through the computational homogenization approach presented in the next subsection.

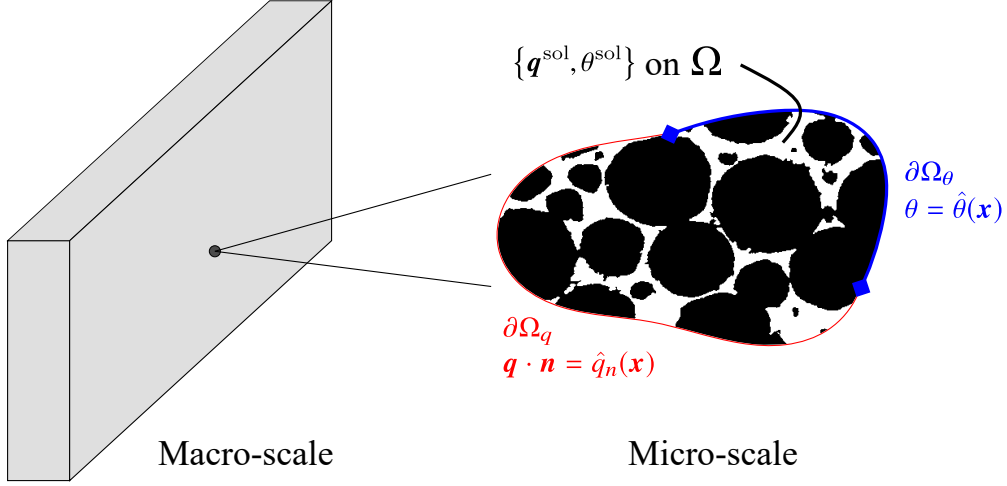


Figure 5: An illustration of two-scale problem. At the micro-scale, boundary temperatures $\hat{\theta}$ and normal heat fluxes \hat{q}_n are prescribed on parts of the boundary $\partial\Omega_q$ and $\partial\Omega_\theta$ respectively, giving solution fields q^{sol} and θ^{sol} over the entire domain Ω .

3.1.2. Micro-scale problem and maximum entropy principle

The micro-scale problem considers the foam as a two-phase domain Ω with boundary $\partial\Omega$, sufficiently large compared to the characteristic microscopic length scale ℓ , yet sufficiently small compared to the macroscopic length scale (see Figure 5). As such, the temperature variations within Ω are small: $T = T_0 + \theta \approx T_0$, with T_0 being the reference temperature and θ the relative temperature. The second-order local thermal conductivity tensor \mathbf{k} is then assumed constant with respect to temperature.

Under steady-state heat conduction with no volumetric heat generation, the micro-scale heat flux vector \mathbf{q} and relative temperature θ are linked by the micro-scale Fourier's law:

$$\mathbf{q} = -\mathbf{k} \cdot \nabla\theta \quad \text{with} \quad \nabla \cdot \mathbf{q} = 0 \quad (4)$$

Given a set of micro-scale boundary conditions on $\partial\Omega$, the heat flux and temperature fields over Ω may be provided by the “maximum entropy principle” introduced by Onsager [39] and formalized in the next paragraph.

Maximum entropy principle. For a set of boundary conditions applied to the domain Ω , it is possible to define the disjoint parts of the boundary $\partial\Omega_q$ and $\partial\Omega_\theta$ on which the boundary normal heat flux \hat{q}_n and temperature $\hat{\theta}$ are prescribed respectively (see Figure 5). The resulting solution heat flux and temperature fields are denoted q^{sol} and θ^{sol} .

An “admissible” solution for the heat flux field q^{adm} is a field that satisfies the boundary heat flux conditions, while possibly differing from the “true” solution q^{sol} elsewhere. The maximum

entropy principle states that q^{sol} maximizes the rate of entropy increase minus the dissipation-rate [39], which for small temperature variations ($T \approx T_0$ on Ω) is written using the functional \mathcal{S} :

$$\forall \mathbf{q} \in \{\mathbf{q}^{\text{adm}}\}, \quad \mathcal{S}(\mathbf{q}) = \frac{1}{T_0^2} \left(- \int_{\partial\Omega_\theta} (\mathbf{q} \cdot \mathbf{n}) \hat{\theta} \, dA - \frac{1}{2} \int_{\Omega} \mathbf{q} \cdot (\mathbf{k}^{-1} \cdot \mathbf{q}) \, dV \right) \leq \mathcal{S}(\mathbf{q}^{\text{sol}}) \quad (5)$$

where $\hat{\theta}$ is the boundary temperature prescribed on $\partial\Omega_\theta$.

Similarly, an ‘‘admissible’’ solution θ^{adm} for the temperature field satisfies the temperature boundary conditions, but may differ from the ‘‘true’’ solution θ^{sol} elsewhere. The complementary statement of the maximum entropy principle is written as:

$$\forall \theta \in \{\theta^{\text{adm}}\}, \quad \mathcal{S}_c(\theta) = \frac{1}{T_0^2} \left(- \int_{\partial\Omega_q} \hat{q}_n \theta \, dA - \frac{1}{2} \int_{\Omega} (\mathbf{k} \cdot \nabla \theta) \cdot \nabla \theta \, dV \right) \leq \mathcal{S}_c(\theta^{\text{sol}}) \quad (6)$$

where \hat{q}_n is the boundary normal heat flux prescribed on $\partial\Omega_q$.

Note that for a given set of boundary conditions and the resulting solution fields $\{\mathbf{q}^{\text{sol}}, \theta^{\text{sol}}\}$, the following property may be proven with the divergence theorem (equation (A.1)):

$$\begin{aligned} \mathcal{S}(\mathbf{q}^{\text{sol}}) + \mathcal{S}_c(\theta^{\text{sol}}) &= \frac{1}{T_0^2} \left(- \int_{\partial\Omega} (\mathbf{q}^{\text{sol}} \cdot \mathbf{n}) \theta^{\text{sol}} \, dA + \int_{\Omega} \mathbf{q}^{\text{sol}} \cdot \nabla \theta^{\text{sol}} \, dV \right) = 0 \\ &\iff \mathcal{S}(\mathbf{q}^{\text{sol}}) = -\mathcal{S}_c(\theta^{\text{sol}}) \end{aligned} \quad (7)$$

3.1.3. Micro-macro scale transition and macrohomogeneity condition

The following averaging relation is proposed for any given scalar or vector field defined over Ω :

$$\langle \bullet \rangle = \frac{1}{V} \int_{\Omega} \bullet \, dV \quad (8)$$

Having obtained the solution heat flux and temperature fields, the micro-macro scale transition is achieved by assigning $\mathbf{F} \equiv \langle \mathbf{q} \rangle$ and $\mathbf{G} \equiv \langle \nabla \theta \rangle$ [18, 19]. The terms ‘‘mean’’ and ‘‘macroscopic’’ are henceforth used interchangeably. It is then possible to identify a second-order apparent thermal conductivity (ATC) tensor \mathbf{k}_{app} linking \mathbf{F} and \mathbf{G} , using the macroscopic Fourier’s law (given here in both tensorial notation and vector/matrix form with respect to the Cartesian frame):

$$\mathbf{F} = -\mathbf{k}_{\text{app}} \cdot \mathbf{G} \quad \equiv \quad \begin{bmatrix} F_1 \\ F_2 \\ F_3 \end{bmatrix} = - \begin{bmatrix} k_{11}^{\text{app}} & k_{12}^{\text{app}} & k_{13}^{\text{app}} \\ k_{21}^{\text{app}} & k_{22}^{\text{app}} & k_{23}^{\text{app}} \\ k_{31}^{\text{app}} & k_{32}^{\text{app}} & k_{33}^{\text{app}} \end{bmatrix} \begin{bmatrix} G_1 \\ G_2 \\ G_3 \end{bmatrix} \quad (9)$$

As \mathbf{k}_{app} may vary depending on the choice of micro-scale boundary conditions and the size of Ω , it is generally different from \mathbf{k}_{eff} , which should be intrinsic to the homogenized medium. The chosen micro-scale boundary conditions to compute \mathbf{k}_{app} should ensure consistency of fundamental thermodynamic quantities between the micro- and macro-scales. This ‘‘macrohomogeneity condition’’ is detailed below.

Macrohomogeneity condition. The following quantity represents the micro-scale specific entropy production rate due to the irreversibility of heat conduction, and is obtained by expressing the second law of thermodynamics in the form of the Clausius-Duhem inequality [39, 40]:

$$-\mathbf{q} \cdot \frac{\nabla T}{T^2} \geq 0 \quad (10)$$

where $T = T_0 + \theta$. Note that the same quantity appears in the statements of the maximum entropy principle (equations (5) and (6)).

The macrohomogeneity condition states that the specific entropy production rate should be conserved between the micro- and macro-scales [19, 23]. For small temperature variations ($T \approx T_0$) across Ω , this condition can be simplified to:

$$\left\langle -\mathbf{q} \cdot \frac{\nabla T}{T^2} \right\rangle \approx \left\langle -\mathbf{q} \cdot \frac{\nabla \theta}{T_0^2} \right\rangle = -\mathbf{F} \cdot \frac{\mathbf{G}}{T_0^2} \iff \langle \mathbf{q} \cdot \nabla \theta \rangle \approx \mathbf{F} \cdot \mathbf{G} \quad (11)$$

Schindler et al. [23] showed that this simplification is indeed valid, inducing an error of 0.18% when the maximal temperature variation over the domain is 1 K for $273 \text{ K} \leq T_0 \leq 775 \text{ K}$.

As the divergence theorem links the averages $\langle \mathbf{q} \rangle$, $\langle \nabla \theta \rangle$, and $\langle \mathbf{q} \cdot \nabla \theta \rangle$ to their boundary values (see equation (A.1)), the applied boundary conditions have a direct influence on whether the macrohomogeneity condition is satisfied.

3.2. Boundary conditions

The different sets of boundary conditions considered in this work are presented in this section, and their validity with respect to the macrohomogeneity condition is examined. For mathematical details, readers may refer to Appendix A.

3.2.1. Uniform and periodic boundary conditions

The usual uniform and periodic boundary conditions encountered in the literature on computational homogenization (e.g., [19, 27]) are first discussed.

Uniform heat flux (UHF). Denoting \mathbf{F}_0 an arbitrary heat flux vector constant with respect to \mathbf{x} , the normal component of the heat flux $q_n = \mathbf{q} \cdot \mathbf{n}$ at all points on the boundary is fixed:

$$\forall \mathbf{x} \in \partial\Omega, \quad q_n = \mathbf{F}_0 \cdot \mathbf{n} \quad (12)$$

These conditions can be applied to computational domains of any geometry, and lead to: $\langle \mathbf{q} \rangle = \mathbf{F}_0$. Application of these boundary conditions automatically satisfies the simplified macrohomogeneity condition (11).

Uniform temperature gradient (UTG). Denoting \mathbf{G}_0 an arbitrary temperature gradient vector constant with respect to \mathbf{x} , the temperature θ at all points on the boundary is fixed:

$$\forall \mathbf{x} \in \partial\Omega, \quad \theta = \mathbf{G}_0 \cdot \mathbf{x} \quad (13)$$

As with the UHF, these conditions can be applied to computational domains of any geometry, and lead to: $\langle \nabla \theta \rangle = \mathbf{G}_0$. Application of these boundary conditions also automatically satisfies the simplified macrohomogeneity condition (11).

Periodic boundary conditions (PBC). These conditions are based on splitting the temperature field over the entire domain into $\theta = \mathbf{G}_0 \cdot \mathbf{x} + \tilde{\theta}$, and imposing the periodicity on $\tilde{\theta}$ (which represents the fluctuations due to the heterogeneities). In practice, for cuboidal domains, the boundary temperature is specified as:

$$\forall \{\mathbf{x}^+, \mathbf{x}^-\} \in \partial\Omega, \quad \theta(\mathbf{x}^+) = \theta(\mathbf{x}^-) + \mathbf{G}_0 \cdot (\mathbf{x}^+ - \mathbf{x}^-) \quad (14)$$

where \mathbf{x}^+ and \mathbf{x}^- are two homologous points on the boundary $\partial\Omega$, i.e., one point is obtained by projecting the other along the normal vector onto the opposite face. If a variational approach such as the finite element method is used to resolve the temperature and heat flux fields within the domain, application of the PBC automatically results in antiperiodic normal heat fluxes ($q_n(\mathbf{x}^+) = -q_n(\mathbf{x}^-)$) on the boundary [41]. If that is not the case, this needs to be specified as an additional constraint (e.g., in [14]).

Application of the PBC also automatically satisfies the simplified macrohomogeneity condition (11). The PBC as defined do not explicitly impose any restriction (e.g, periodicity) on the geometry of the computational domain [19]. However, their use on non-periodic microstructures such as real foam models reconstructed with X-ray tomography could lead to errors in the computed ATC [30].

3.2.2. Mixed boundary conditions and validity criteria

Unlike uniform and periodic boundary conditions, mixed boundary conditions (MBC) do not generally satisfy the macrohomogeneity condition (equation (11)), and are thus rarely considered within the computational homogenization framework. In this subsection, the validity of a set of MBC commonly encountered in past work on porous media [1, 2, 13, 31] and sporadically used in computational homogenization [21, 24] is analysed with respect to the macrohomogeneity condition.

Definition of the MBC. Consider a cuboidal domain Ω centered at the origin of the Cartesian frame, with boundary normal vectors \mathbf{n} aligned to the Cartesian axes $\{\mathbf{e}_1, \mathbf{e}_2, \mathbf{e}_3\}$ (see Figure 6). The lengths of the cuboid along the \mathbf{e}_1 , \mathbf{e}_2 and \mathbf{e}_3 directions are denoted L_1 , L_2 and L_3 respectively. Assuming $\mathbf{G}_0 = G_0 \mathbf{e}_1$, the MBC are defined as follows (the cases with \mathbf{e}_1 replaced by \mathbf{e}_2 and \mathbf{e}_3 are obtained trivially by index permutation):

$$\forall \mathbf{x} \in \partial\Omega, \quad \begin{cases} \theta = \mathbf{G}_0 \cdot \mathbf{x} = G_0 x_1 & \text{if } \mathbf{n} \parallel \mathbf{G}_0 \\ q_n = 0 & \text{if } \mathbf{n} \perp \mathbf{G}_0 \end{cases} \quad (15)$$

To simplify the expressions for the macroscopic fields, the following notations are defined:

$$\forall j \in \{1, 2, 3\}, \quad \begin{cases} \partial\Omega_j^+ = \{\mathbf{x} \in \partial\Omega \mid \mathbf{n} = +\mathbf{e}_j\} \\ \partial\Omega_j^- = \{\mathbf{x} \in \partial\Omega \mid \mathbf{n} = -\mathbf{e}_j\} \\ \partial\Omega_j = \partial\Omega_j^+ \cup \partial\Omega_j^- \end{cases} \quad (16)$$

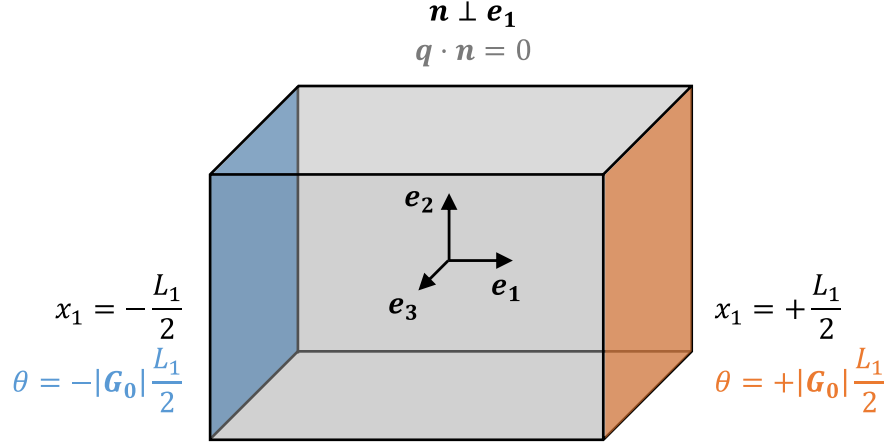


Figure 6: Schema of the mixed boundary conditions (MBC) applied to a cuboidal domain.

The macroscopic fields are obtained by directly applying their definitions in boundary integral form (equations (A.3) to (A.5) in Appendix A). The macroscopic heat flux vector is expressed as:

$$[\mathbf{F}] = \begin{bmatrix} F_1 = \frac{1}{V} \left(\int_{\partial\Omega_1^+} q_1 \frac{L_1}{2} dx_2 dx_3 - \int_{\partial\Omega_1^-} q_1 \left(-\frac{L_1}{2}\right) dx_2 dx_3 \right) \\ F_2 = \frac{1}{V} \left(\int_{\partial\Omega_1^+} q_1 x_2 dx_2 dx_3 - \int_{\partial\Omega_1^-} q_1 x_2 dx_2 dx_3 \right) \\ F_3 = \frac{1}{V} \left(\int_{\partial\Omega_1^+} q_1 x_3 dx_2 dx_3 - \int_{\partial\Omega_1^-} q_1 x_3 dx_2 dx_3 \right) \end{bmatrix} \quad (17)$$

The macroscopic temperature gradient is expressed as:

$$[\mathbf{G}] = \begin{bmatrix} G_1 = \frac{G_0}{V} \left(\int_{\partial\Omega_1^+} \frac{L_1}{2} dx_2 dx_3 - \int_{\partial\Omega_1^-} \left(-\frac{L_1}{2}\right) dx_2 dx_3 \right) = G_0 \\ G_2 = \frac{1}{V} \left(\int_{\partial\Omega_2^+} \theta dx_1 dx_3 - \int_{\partial\Omega_2^-} \theta dx_1 dx_3 \right) \\ G_3 = \frac{1}{V} \left(\int_{\partial\Omega_3^+} \theta dx_1 dx_2 - \int_{\partial\Omega_3^-} \theta dx_1 dx_2 \right) \end{bmatrix} \quad (18)$$

The macroscopic specific entropy production rate is expressed as:

$$\langle \mathbf{q} \cdot \nabla \theta \rangle = \frac{G_0}{V} \left(\int_{\partial\Omega_1^+} q_1 \frac{L_1}{2} dx_2 dx_3 - \int_{\partial\Omega_1^-} q_1 \left(-\frac{L_1}{2}\right) dx_2 dx_3 \right) = F_1 G_1 \quad (19)$$

Validity criteria. Recall that the MBC do not necessarily satisfy the macrohomogeneity condition given in equation (11), which based on equations (17) to (19) can be rewritten as:

$$\mathbf{F} \cdot \mathbf{G} - \langle \mathbf{q} \cdot \nabla \theta \rangle = 0 \iff F_2 G_2 + F_3 G_3 = 0 \quad (20)$$

While equation (20) can be systematically verified *a posteriori*, it is often desirable to be able to deduce *a priori* if the macrohomogeneity condition is satisfied based on the given microstructure. To begin with, one may observe that a sufficient condition for equation (20) to be satisfied is if the mean temperature difference between any two pairs of opposite lateral faces are zero, which from equation (18) gives:

$$G_2 = G_3 = 0 \quad (21)$$

Equation (21) is hereafter called the sufficient condition for macrohomogeneity of the MBC. For non-periodic foam structures, it can be postulated that if the pores are distributed in space in a statistically homogeneous manner, the macroscopic temperature gradient will deviate little from the \mathbf{e}_1 direction: the temperature fields on opposite lateral faces will then be similar, i.e., the sufficient condition (21) will be satisfied. This postulate will be confirmed by numerical modeling on real and virtual microstructures in subsection 5.4.

Note also that if condition (21) holds, the expression for k_{11}^{app} is consistent with the scalar k_{1D} in equation (1) computed with the 1D simplification to Fourier's law:

$$G_2 = G_3 = 0 \implies k_{11}^{\text{app}} = -\frac{F_1}{G_1} = - \underbrace{\frac{L_1}{V}}_{1/A} \underbrace{\frac{1}{2} \left(\int_{\partial\Omega_1} q_1 dx_2 dx_3 \right)}_{\mathcal{Q}} \underbrace{\frac{1}{G_0}}_{\Delta L / \Delta \theta} \quad (22)$$

This alone by no means implies that \mathbf{k}_{app} is orthotropic, since F_2 and F_3 are not necessarily zero.

3.3. Influence of boundary conditions on the apparent thermal conductivity

If the computational domain chosen for the micro-scale problem is a representative volume element (RVE) of the foam material, the apparent thermal conductivity (ATC, \mathbf{k}_{app}) should then be equal to the effective thermal conductivity (ETC, \mathbf{k}_{eff}) under any set of boundary conditions satisfying the macrohomogeneity condition. However, as the RVE may be prohibitively large for real porous media, it is often necessary to estimate the ETC from smaller, non-representative computational domains. As such, the ATC may vary greatly depending on the boundary conditions used due to edge effects [20, 21, 24].

For foam domains Ω smaller than the RVE, the values of \mathbf{k}_{app} under different boundary conditions are compared analytically using the maximum entropy principle [39] presented in section 3.1.2. The uniform heat flux (UHF), uniform temperature gradient (UTG), periodic (PBC) and mixed (MBC) boundary conditions presented in subsection 3.2 are considered. The objective is to establish order relations between the four values of \mathbf{k}_{app} . As the thermal conductivity tensor is necessarily positive semi-definite [40], any two thermal conductivity tensors \mathbf{k}_A and \mathbf{k}_B may be compared based on their quadratic form:

$$\begin{aligned} \mathbf{k}_A \leq \mathbf{k}_B &\equiv (\mathbf{k}_A \cdot \mathbf{G}_0) \cdot \mathbf{G}_0 \leq (\mathbf{k}_B \cdot \mathbf{G}_0) \cdot \mathbf{G}_0 \quad \forall \mathbf{G}_0 \\ &\equiv \mathbf{F}_0 \cdot (\mathbf{k}_A^{-1} \cdot \mathbf{F}_0) \geq \mathbf{F}_0 \cdot (\mathbf{k}_B^{-1} \cdot \mathbf{F}_0) \quad \forall \mathbf{F}_0 \end{aligned} \quad (23)$$

The discussion is hereinafter restricted to cuboidal domains Ω comprised between points $-[L_1 \ L_2 \ L_3]/2$ and $+[L_1 \ L_2 \ L_3]/2$ in the Cartesian frame $\{\mathbf{e}_1, \mathbf{e}_2, \mathbf{e}_3\}$, as illustrated in Figure 6,

with the arbitrary heat flux and temperature gradient vectors $\mathbf{F}_0 = F_0 \mathbf{e}_1$ and $\mathbf{G}_0 = G_0 \mathbf{e}_1$ (the cases with \mathbf{e}_1 replaced with \mathbf{e}_2 and \mathbf{e}_3 can be obtained trivially by index permutation). The same reference temperature T_0 is adopted for all four boundary value problems. It is first assumed that application of the MBC satisfies the macrohomogeneity condition (20) (but not necessarily condition (21), the sufficient condition for macrohomogeneity).

3.3.1. Known order relations

Key results from the literature [17, 19, 22, 24, 42] are summarized below, with complete demonstrations included in Appendix B. These are based on the observation that any heat flux \mathbf{q} defined over Ω is an admissible solution heat flux field to the UTG problem, since no boundary heat fluxes are prescribed ($\partial\Omega_q = \emptyset$). Conversely, any temperature θ defined over Ω is an admissible solution temperature field to the UHF problem since no boundary temperatures are defined ($\partial\Omega_\theta = \emptyset$). The maximum entropy principle (5) and its complementary statement (6) then give:

$$\forall \mathbf{q}, \quad \mathcal{S}^{\text{UTG}}(\mathbf{q}) \leq \mathcal{S}^{\text{UTG}}(\mathbf{q}^{\text{UTG}}) \quad (24a)$$

$$\forall \theta, \quad \mathcal{S}_c^{\text{UHF}}(\theta) \leq \mathcal{S}_c^{\text{UHF}}(\theta^{\text{UHF}}) \quad (24b)$$

Firstly, considering the true solutions to the PBC problem \mathbf{q}^{PBC} and θ^{PBC} as admissible solutions to the UTG and UHF problems respectively, equations (24) gives a well-known result [17, 19, 24] the demonstration of which is found in Appendix B:

$$\begin{cases} \mathcal{S}^{\text{UTG}}(\mathbf{q}^{\text{PBC}}) \leq \mathcal{S}^{\text{UTG}}(\mathbf{q}^{\text{UTG}}) \\ \mathcal{S}_c^{\text{UHF}}(\theta^{\text{PBC}}) \leq \mathcal{S}_c^{\text{UHF}}(\theta^{\text{UHF}}) \end{cases} \iff \mathbf{k}_{\text{app}}^{\text{UHF}} \leq \mathbf{k}_{\text{app}}^{\text{PBC}} \leq \mathbf{k}_{\text{app}}^{\text{UTG}} \quad (25)$$

Secondly, considering the true solutions to the MBC problem \mathbf{q}^{MBC} and θ^{MBC} as admissible solutions to the UTG and UHF problems respectively, a development based on the work of Hazanov and Huet [42] gives the following result, which is also demonstrated in Appendix B:

$$\begin{cases} \mathcal{S}^{\text{UTG}}(\mathbf{q}^{\text{MBC}}) \leq \mathcal{S}^{\text{UTG}}(\mathbf{q}^{\text{UTG}}) \\ \mathcal{S}_c^{\text{UHF}}(\theta^{\text{MBC}}) \leq \mathcal{S}_c^{\text{UHF}}(\theta^{\text{UHF}}) \end{cases} \iff \mathbf{k}_{\text{app}}^{\text{UHF}} \leq \mathbf{k}_{\text{app}}^{\text{MBC}} \leq \mathbf{k}_{\text{app}}^{\text{UTG}} \quad (26)$$

Since $\mathbf{k}_{\text{app}}^{\text{UHF}} = \mathbf{k}_{\text{eff}} = \mathbf{k}_{\text{app}}^{\text{UTG}}$ when $V \rightarrow \infty$ according to Hill [22], the following relation necessarily holds for sufficiently large volumes:

$$\mathbf{k}_{\text{app}}^{\text{UHF}} \leq \mathbf{k}_{\text{eff}} \leq \mathbf{k}_{\text{app}}^{\text{UTG}} \quad (27)$$

In summary, the existing literature agrees that the UTG and UHF yield upper- and lower-bound estimates respectively for \mathbf{k}_{eff} , and for any given domain size, the PBC and MBC (assuming the macrohomogeneity condition (20) holds for the latter) provide equally good if not better estimates. However, no direct theoretical comparison has been made between the estimates obtained with the PBC and MBC, a gap which will be addressed presently.

3.3.2. Comparison between mixed and periodic boundary conditions

Assume for the purpose of the present demonstration that there exists a cuboidal domain Ω that, when subjected to the PBC, gives zero normal heat fluxes on the lateral faces (for foam geometries, this premise is in fact more general than it may seem at first glance, as will be explained following the demonstration). For the considered microstructure, \mathbf{q}^{PBC} is thus an admissible solution heat flux to the MBC problem, and one may write:

$$\begin{aligned}
& \mathcal{S}^{\text{MBC}}(\mathbf{q}^{\text{PBC}}) \leq \mathcal{S}^{\text{MBC}}(\mathbf{q}^{\text{MBC}}) \\
\iff & - \int_{\partial\Omega_1} (\mathbf{q}^{\text{PBC}} \cdot \mathbf{n})(\mathbf{G}_0 \cdot \mathbf{x}) \, dA - \frac{V}{2} \langle \mathbf{q} \rangle^{\text{PBC}} \cdot \left((\mathbf{k}_{\text{app}}^{\text{PBC}})^{-1} \cdot \langle \mathbf{q} \rangle^{\text{PBC}} \right) \\
& \leq - \int_{\partial\Omega_1} (\mathbf{q}^{\text{MBC}} \cdot \mathbf{n})(\mathbf{G}_0 \cdot \mathbf{x}) \, dA - \frac{V}{2} \langle \mathbf{q} \rangle^{\text{MBC}} \cdot \left((\mathbf{k}_{\text{app}}^{\text{MBC}})^{-1} \cdot \langle \mathbf{q} \rangle^{\text{MBC}} \right) \quad (28) \\
\iff & -V \langle \mathbf{q} \rangle^{\text{PBC}} \cdot \mathbf{G}_0 + \frac{V}{2} \langle \mathbf{q} \rangle^{\text{PBC}} \cdot \langle \nabla \theta \rangle^{\text{PBC}} \\
& \leq -V \langle \mathbf{q} \rangle^{\text{MBC}} \cdot \mathbf{G}_0 + \frac{V}{2} \langle \mathbf{q} \rangle^{\text{MBC}} \cdot \langle \nabla \theta \rangle^{\text{MBC}}
\end{aligned}$$

Assuming now that the sufficient condition for macrohomogeneity (21) holds for the MBC, i.e., $\langle \nabla \theta \rangle^{\text{MBC}} = \mathbf{G}_0$, and substituting $\langle \mathbf{q} \rangle = -\mathbf{k}_{\text{app}} \cdot \langle \nabla \theta \rangle$, the following inequality is obtained from equation (28):

$$\begin{aligned}
& -\frac{V}{2} \langle \mathbf{q} \rangle^{\text{PBC}} \cdot \mathbf{G}_0 \leq -\frac{V}{2} \langle \mathbf{q} \rangle^{\text{MBC}} \cdot \mathbf{G}_0 \\
\iff & \left(\mathbf{k}_{\text{app}}^{\text{PBC}} \cdot \mathbf{G}_0 \right) \cdot \mathbf{G}_0 \leq \left(\mathbf{k}_{\text{app}}^{\text{MBC}} \cdot \mathbf{G}_0 \right) \cdot \mathbf{G}_0 \quad (29) \\
& \iff \mathbf{k}_{\text{app}}^{\text{PBC}} \leq \mathbf{k}_{\text{app}}^{\text{MBC}}
\end{aligned}$$

The premise of zero normal heat fluxes on the lateral faces ($q_n^{\text{PBC}} = 0$ where $\mathbf{n} \perp \mathbf{G}_0$) required for equations (28) and (29) to hold can in fact be generalized to most types of foam geometries considered. It is trivially met for periodic microstructures for which the lateral boundaries are symmetry planes (e.g., unit cells such as in [24]). For non-periodic highly porous foam geometries, the following postulate can be offered: under the PBC, as q_n^{PBC} is anti-periodic, only opposite pairs of boundary points that both belong to the solid phase would have non-zero heat fluxes (in porous media, near-zero heat fluxes are found at points on the boundary where the pore phase is present and where the heat flux is not specified [24]). With increasing porosity, the rate of occurrence of such points decreases sharply, reducing the normal heat flux to zero everywhere on the lateral faces (save eventually for a few points).

In summary, for periodic geometries with boundary faces as symmetry planes and non-periodic foam models with sufficiently high boundary mismatch, the premise $q_n^{\text{PBC}} = 0$ where $\mathbf{n} \perp \mathbf{G}_0$ should hold. These postulates will be examined through the numerical case studies (sections 5.2 and 5.4).

Combining equation (29) with the inequalities in equations (25) and (26) gives:

$$\mathbf{k}_{\text{app}}^{\text{UHF}} \leq \mathbf{k}_{\text{app}}^{\text{PBC}} \leq \mathbf{k}_{\text{app}}^{\text{MBC}} \leq \mathbf{k}_{\text{app}}^{\text{UTG}} \quad (30)$$

While $\mathbf{k}_{\text{app}}^{\text{PBC}}$ is equal to the effective thermal conductivity \mathbf{k}_{eff} in the case of periodic geometries, no rigorous ETC solution is available for non-periodic geometries, for which $\mathbf{k}_{\text{app}}^{\text{PBC}}$ and $\mathbf{k}_{\text{app}}^{\text{MBC}}$ can only be considered the best possible estimates of \mathbf{k}_{eff} . One key goal of the numerical studies presented in the subsequent sections is to ascertain which of the two are more appropriate for the different types of foam geometries considered.

4. Numerical methods

Finite element modeling was performed on the different types of cubic foam geometries ($L_1 = L_2 = L_3 = L$) described in section 2 with two key goals:

- to investigate the validity, accuracy and precision of the effective thermal conductivity (ETC, \mathbf{k}_{eff}) estimated with the apparent thermal conductivity (ATC, \mathbf{k}_{app}) under different boundary conditions on foam geometries smaller than the representative volume element (RVE), and
- to verify the theoretical postulates of section 3 pertaining to the validity of the mixed boundary conditions (MBC) and to the comparison of its result and that obtained under periodic boundary conditions (PBC).

The finite element modeling procedure is described in subsection 4.1. The quantities of interest during post-processing (notably the concepts of validity, accuracy, and precision) are defined in subsection 4.2. The precision of the estimated ETC for random microstructures can be evaluated with a statistical treatment based on the integral range [20], detailed in section 4.3.

4.1. Finite element modeling procedure

Initially represented in binary voxel format of equal voxel size (8.75 μm), the different cubic geometries were fully meshed with linear (P1) brick elements with a mesh density of one element per voxel (see Figure 7(a)); it was verified that further mesh refinement did not modify the computed ATC value by more than 1.6% on average. Each element was attributed a constant isotropic thermal conductivity corresponding to that of sintered alumina [43] or air [44] at a reference temperature $T_0 = 298$ K. The contrast between the solid and pore phase conductivities (k_s and k_p respectively) is indeed very high: $k_s/k_p = 539$.

Finite element modeling of 3D steady-state heat transfer over the entire computational domain was performed using the preconditioned Krylov-based iterative solver of Abaqus/Standard 2017 [45]. The governing variational statement of the finite element method [41, 45, 46] is mathematically equivalent to the maximum entropy principle [39] presented in section 3.1.2. From the computed temperature and heat flux fields (see example in Figures 7(b)–(c)), the mean temperature gradient, heat flux, and specific entropy production rate were calculated based on their respective definitions in Appendix A.

To solve for \mathbf{k}_{app} , three orthogonal configurations were solved for each boundary value problem, i.e., the directions of $\mathbf{G}_0 = G_0 \mathbf{e}_j$ or $\mathbf{F}_0 = F_0 \mathbf{e}_j$ were permuted for $j \in \{1, 2, 3\}$. As equation (9) gives three equations linking $\mathbf{F} \equiv \langle \mathbf{q} \rangle$ and $\mathbf{G} \equiv \langle \nabla \theta \rangle$ for each configuration, nine equations were thus obtained to solve for the nine unknowns in \mathbf{k}_{app} . With MPI-based parallelization on a quad-core processor with a clock speed of 2.20 GHz, computation of the complete ATC tensor

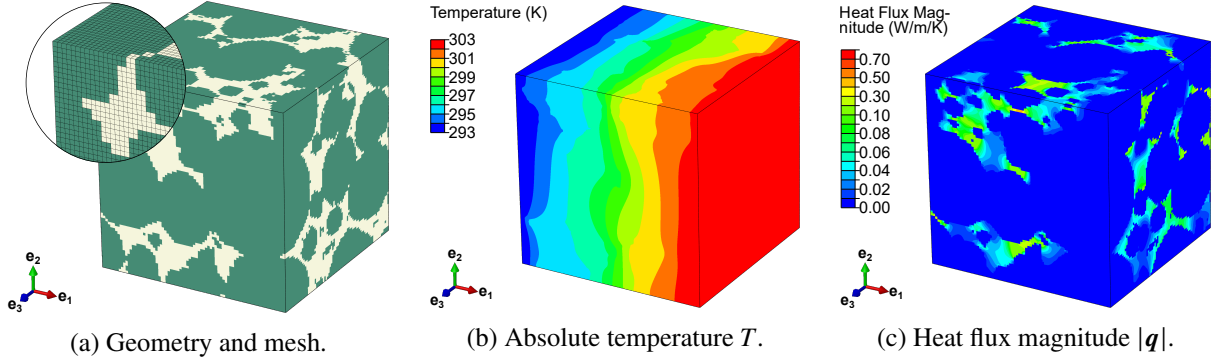


Figure 7: Application of the mixed boundary condition (MBC) on a $1.35 \text{ mm} \times 1.35 \text{ mm} \times 1.35 \text{ mm}$ reconstructed foam model meshed with 3.65 million (154^3) elements. The $\partial\Omega_1^+$, $\partial\Omega_2^+$, and $\partial\Omega_3^+$ faces are shown.

for a domain with 8 million elements took approximately three hours, half of which was spent on post-processing.

4.2. Quantities of interest during post-processing

For each set of boundary conditions and each type of microstructure, four aspects of the computed ATC are studied:

Validity with respect to the macrohomogeneity condition. As small temperature variations are considered, the macrohomogeneity condition (11) should be satisfied by each set of boundary conditions used for the resulting ATC to be considered valid. An “entropy residual” r_S can be defined as follows:

$$r_S = \sqrt{\frac{1}{3} \sum_{j=1}^3 \left(\frac{\langle \mathbf{q} \cdot \nabla \theta \rangle - \mathbf{F} \cdot \mathbf{G}}{\mathbf{F} \cdot \mathbf{G}} \right)_{G_0 \parallel e_j}^2} \quad (31)$$

A zero value of r_S means that the macrohomogeneity condition (11) is satisfied, i.e., the specific entropy production rate is consistent between the micro- and macro-scales.

Diagonalizability. Eigendecomposition of the ATC was performed to identify the principal directions of orthotropy (if they exist) and the ATC along these directions. Consider a cubic domain aligned to the Cartesian frame in which the ATC matrix $[\mathbf{k}_{\text{app}}]$ is computed. If the thermal conductivity of the underlying material is indeed orthotropic in another reference frame rotated with respect to the Cartesian frame by a matrix $[\mathbf{R}]$, then $[\mathbf{k}_{\text{app}}]$ is diagonalizable and the diagonalized ATC matrix $[\mathbf{k}_{\text{app}}^D]$ can be written as:

$$[\mathbf{k}_{\text{app}}^D] = [\mathbf{R}]^{-1} [\mathbf{k}_{\text{app}}] [\mathbf{R}] \quad \text{with} \quad [\mathbf{k}_{\text{app}}^D] = \begin{bmatrix} k_{\text{I}}^{\text{app}} & 0 & 0 \\ 0 & k_{\text{II}}^{\text{app}} & 0 \\ 0 & 0 & k_{\text{III}}^{\text{app}} \end{bmatrix} \quad (32)$$

where $k_{\text{I}}^{\text{app}}$, $k_{\text{II}}^{\text{app}}$ and $k_{\text{III}}^{\text{app}}$ are the real eigenvalues of $[\mathbf{k}_{\text{app}}]$, and the columns of $[\mathbf{R}]$ are the corresponding eigenvectors.

Accuracy. For periodic geometries, the ATC obtained through application of the PBC is the reference ETC ($\mathbf{k}_{\text{app}}^{\text{PBC}} = \mathbf{k}_{\text{eff}}$), and was used to evaluate the accuracy of those obtained under the other boundary conditions (UHF, UTG, MBC). For non-periodic geometries, no rigorous reference ETC can be obtained in general, if convergence of the UHF and UTG bounds is not achieved.

Precision. While deterministic effective properties exist for regular geometries, for random microstructures, the variation between the ATC may not vanish even when the computational domain is extremely large. The ETC was therefore estimated using the stochastic mean ATC $\langle\langle \mathbf{k}_{\text{app}} \rangle\rangle$ of different samples of the material (or realizations, if digitally generated virtual geometries are considered). With N independent samples of equal volume V , the precision ϵ of the ij term of the mean ATC matrix was evaluated from the standard error [20]:

$$\epsilon = \frac{2\sigma_k}{\langle\langle k_{ij}^{\text{app}} \rangle\rangle \sqrt{N}} \quad (33)$$

where σ_k is the standard deviation of the ATC, which generally decreases with increasing V . To achieve a given precision ϵ , one may either work with a large number of small samples, or a small number of large samples.

4.3. Statistical treatment based on the integral range

In random foams of arbitrary size, the interplay between the variance of the ATC and sample volume depends not only on the regularity of the microstructure, but also on the type of property considered, the phase contrast, and the boundary conditions. To account for their influence, Kanit et al. [20] proposed the following power law model for the ATC variance σ_k^2 :

$$\sigma_k^2 = f_p(1 - f_p)(k_s - k_p)^2 \left(\frac{J_k}{V}\right)^\alpha \quad \text{for } V \gg J_k \quad (34)$$

where k_s and k_p are the conductivities of the solid and pore phases respectively, α is the power law exponent, and J_k is the integral range which can be interpreted as the scale of the phenomenon, V being the scale of observation. In practice, for a given set of boundary conditions and microstructure, J_k and α are estimated by first computing σ_k for a few different values of V , then performing a power law regression.

With equations (33) and (34), it is then possible to evaluate the precision ϵ of the estimated ETC even if computation of the standard deviation is impossible (e.g., when an insufficient number of samples are available). Alternatively, one may also define a target precision ϵ_0 , and estimate the associated ‘‘statistical RVE size’’ as $V(\epsilon_0, N = 1)$.

It is important to note that application of the statistical treatment only accounts for the scatter due to the random microstructure; when working with geometries of sub-RVE sizes, due to edge effects, inaccuracies in the ETC estimate may still exist depending on the chosen boundary conditions.

5. Results and Discussion

The apparent thermal conductivity (ATC, k_{app}) of three types of foam geometries are computed under four sets of boundary conditions: uniform heat flux (UHF), uniform temperature gradient (UTG), periodic (PBC) and mixed (MBC) boundary conditions. While a deterministic value of the effective thermal conductivity (ETC, k_{eff}) intrinsic to the entire medium may be computed for regular periodic microstructures, for random microstructures, the mean ATC of several realizations was used as an estimate of the ETC.

Specific results corresponding to each type of foam geometry are first presented:

- Subsection 5.1 describes a preliminary study on unit cell-based geometries that highlights the effect of geometrical non-periodicity on the accuracy of the estimated ETC;
- Subsection 5.2 describes a study of the effect of random porosity on the accuracy of the ETC estimated under different boundary conditions in the case of periodic virtual foams;
- Subsection 5.3 describes a study of the accuracy and precision of the ETC estimated under different boundary conditions on non-periodic tomography-reconstructed real foams.

Last but not least, the theoretical postulates in section 3 pertaining to the validity of the MBC as well as the order relation between the MBC and PBC results are verified in subsection 5.4.

As was commonly done for porous media, the results were given in terms of the normalized ATC k_{app}/k_s , which is generally only dependent on the microstructure and independent of the base material properties due to the high phase contrast [6], allowing the discussion hereafter to be generalized to all foams of similar morphology whatever the base material.

Where appropriate, the results are compared to several well-known analytical models: the series and parallel models, also known as the Wiener or Voigt-Reuss bounds of the ETC of arbitrary mixtures; the Maxwell-Eucken models, also known as the Hashin-Shtrikman bounds for isotropic mixtures; and a power law solution to the “asymmetric” Bruggeman approximation for spherical inclusions of negligible conductivity, commonly named after Archie [47]. A thorough review of analytical models applicable to porous ceramics can be found in references [6] and [7].

5.1. Study on unit cell-based geometries: effect of geometrical non-periodicity

The ATC of the reference orthotropic unit cell (Figure 4(c)) was first calculated using different boundary conditions. Regardless of the boundary conditions used, the ATC matrix was indeed diagonal as expected. Results for two different tessellation sizes are shown in Figure 8. Larger tessellations were not considered to keep the size of the computational domain representative of typical reconstructed foam models.

As the geometry is periodic, the PBC result on a single unit cell directly gives the reference ETC of the whole medium. The conclusions regarding the other boundary conditions were in line with past findings [17, 20, 24]. The UHF and UTG provided lower- and upper-bound estimates of the ETC respectively; however the large difference between the bounds and their extremely slow size convergence due to the large phase contrast render their use impractical, and demonstrate that the RVE as defined by Hill [22] would be prohibitively large. Notably, the UTG result coincides exactly with the parallel model (upper Wiener bound) and seems insensitive to material orthotropy,

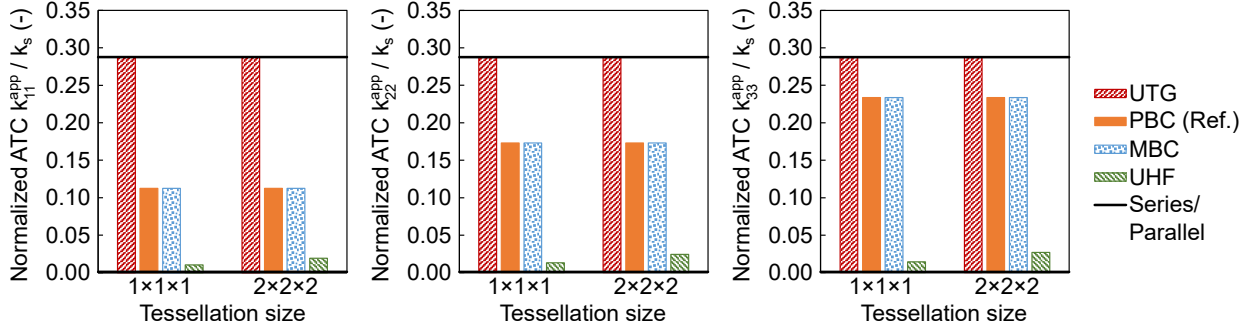


Figure 8: Diagonal values of the apparent thermal conductivity (ATC) matrix computed for two tessellations of the orthotropic unit cell with the uniform heat flux (UHF), uniform temperature gradient (UTG), periodic (PBC), and mixed (MBC) boundary conditions. The bounds given by the series and parallel models are also included; the lower bound (series model) is extremely close to zero.

a recurring observation in the following subsections. Similar to the results of Jiang et al. [24], the ATC of the orthotropic unit cell computed with the MBC is identical to that of the PBC within numerical accuracy.

With a $2 \times 2 \times 2$ tessellation of the orthotropic unit cell as the reference, two non-periodic, anisotropic geometries of the same volume are then created: a “low anisotropy” case through rotating the base material with respect to the Cartesian frame by 45° about the $[0 \ 0 \ 1]$ axis, and a “high anisotropy” case by a rotation of 57.1° about the $[-0.13 \ 0.38 \ 0.92]$ axis. As mentioned in subsection 2.4, the diagonalized ATC matrices of all three geometries should be equal, i.e., they should have the same eigenvalues (equation (32)). Table 2 lists the eigenvalues of the ATC obtained with the PBC and MBC for the different anisotropic cases, and their mean errors with respect to those of the ETC matrix of the orthotropic unit cell calculated with the PBC.

The negative errors show that the ETC is systematically underestimated by both the PBC and MBC due to boundary effects (linked to the zero lateral normal heat flux for the MBC, and to the geometrical mismatch for the PBC). The estimate obtained with the MBC is however significantly better than that given by the PBC, which contradicts the commonly held view that the PBC offer the best estimate for computational domains of sub-RVE sizes. This can be explained by the following: assuming the sufficient condition for macrohomogeneity (20) is fulfilled, the MBC can be seen as a relaxed form of the PBC, in which the restriction of $\tilde{\theta}(\mathbf{x}^+) = \tilde{\theta}(\mathbf{x}^-)$ (local periodicity) on the lateral faces where $\mathbf{n} \perp \mathbf{G}_0$ is replaced with a weaker condition of $\int \tilde{\theta}(\mathbf{x}^+) dA = \int \tilde{\theta}(\mathbf{x}^-) dA$ (“macroscopic periodicity”). At the same time, without the condition of anti-periodicity of q_n on the faces with $\mathbf{n} \parallel \mathbf{G}_0$, the flux concentration is reduced on these faces. These lead to a lower error in the ETC estimation with the MBC than with the PBC.

5.2. Study on virtual periodic foam models: effect of random porosity

Virtual periodic foam models of six different volumes ranging from $V = 2.74 \text{ mm}^3$ to $V = 11.78 \text{ mm}^3$ were generated with the algorithm of Cunsolo et al. [10] (see subsection 2.3) and used to investigate the effect of random porosity on the estimated ETC. For each sample, rigorous reference values for the ATC can be obtained by applying the PBC; however a scatter in the ATC between different samples still exists due to the random microstructure.

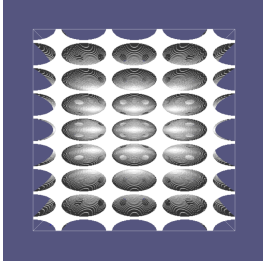
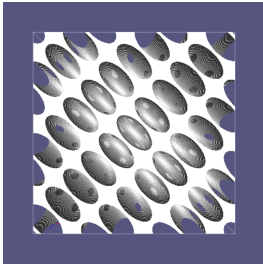
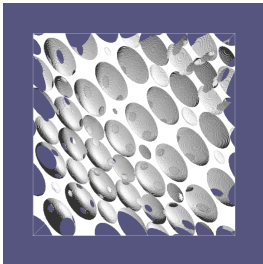
Type of geometry	Normalized ATC matrix [k_{app}/k_s]	Eigenvalues	Mean error
Reference:			
	PBC: $\begin{bmatrix} 0.112 & 0 & 0 \\ 0 & 0.173 & 0 \\ 0 & 0 & 0.234 \end{bmatrix}$ MBC: $\begin{bmatrix} 0.112 & 0 & 0 \\ 0 & 0.173 & 0 \\ 0 & 0 & 0.234 \end{bmatrix}$	$\left\{ \begin{array}{l} 0.112 \\ 0.173 \\ 0.234 \end{array} \right.$ $\left\{ \begin{array}{l} 0.112 \\ 0.173 \\ 0.234 \end{array} \right.$	Ref. 0.0%
Low anisotropy:			
	PBC: $\begin{bmatrix} 0.126 & -0.016 & 0 \\ -0.016 & 0.126 & 0 \\ 0 & 0 & 0.231 \end{bmatrix}$ MBC: $\begin{bmatrix} 0.141 & -0.030 & 0 \\ -0.030 & 0.141 & 0 \\ 0 & 0 & 0.230 \end{bmatrix}$	$\left\{ \begin{array}{l} 0.110 \\ 0.142 \\ 0.231 \end{array} \right.$ $\left\{ \begin{array}{l} 0.111 \\ 0.171 \\ 0.230 \end{array} \right.$	-7.3% -1.5%
High anisotropy:			
	PBC: $\begin{bmatrix} 0.144 & -0.017 & 0.026 \\ -0.017 & 0.127 & 0.024 \\ 0.026 & 0.024 & 0.198 \end{bmatrix}$ MBC: $\begin{bmatrix} 0.112 & -0.020 & 0.027 \\ -0.020 & 0.136 & 0.030 \\ 0.027 & 0.030 & 0.211 \end{bmatrix}$	$\left\{ \begin{array}{l} 0.104 \\ 0.153 \\ 0.211 \end{array} \right.$ $\left\{ \begin{array}{l} 0.107 \\ 0.166 \\ 0.226 \end{array} \right.$	-9.5% -3.9%

Table 2: Normalized apparent thermal conductivity (ATC) matrices of anisotropic geometries computed with periodic (PBC) and mixed (MBC) boundary conditions, and the error of their eigenvalues relative to the reference (Ref.) values.

For each given volume, the mean ATC over 10 virtual foam realizations was used to estimate the ETC of the entire medium. The mean ATC matrices in the Cartesian frame computed with the PBC, MBC and UHF are diagonal, with a slight orthotropy ($\pm 9\%$ difference between the three eigenvalues). The orthotropy is expected from the large scatter observed in the covariance range (see Table 1 in subsection 2.3). The UTG result gives an isotropic matrix with diagonal values equal to the parallel model (upper Wiener bound).

Figure 9 compares the largest eigenvalue of the mean ATC ($k_{\max}^{\text{app}} = \max \{k_{\text{I}}^{\text{app}}, k_{\text{II}}^{\text{app}}, k_{\text{III}}^{\text{app}}\}$) computed with the four sets of boundary conditions, with the precision ϵ indicated as error bands. The precision hovers around 2% for all cases, does not significantly decrease with increasing foam

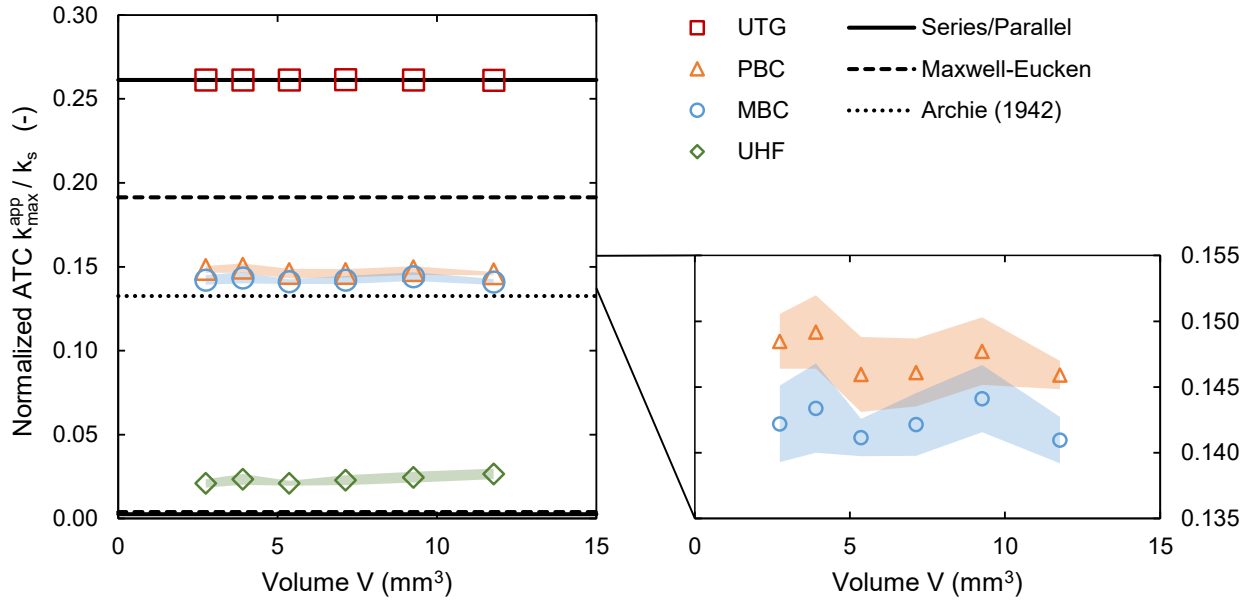


Figure 9: Mean normalized apparent thermal conductivity (ATC) of periodic virtual foams of increasing volume, under uniform heat flux (UHF), uniform temperature gradient (UTG), periodic (PBC) and mixed (MBC) boundary conditions. Comparison was shown for the largest eigenvalue of the ATC. The error bands indicate the standard error.

volume, and is only very slightly lower with the PBC than with the MBC. This is thanks to the similarity in microstructure between the samples: the average over 10 samples of even the smallest volume ($V = 2.74 \text{ mm}^3$) is sufficient to account for the random nature of the virtual foams. Further statistical treatment (e.g., with equation (34)) was thus considered unnecessary.

As the virtual foams are periodic, application of the PBC gives the reference ETC value. As with the orthotropic unit cell, the UTG and UHF yielded extremely wide and thus uninformative upper- and lower-bound estimates of the ETC. Unlike for the orthotropic unit cell, the MBC result is extremely close but systematically lower than the PBC result, which makes this type of geometry a counter-example to the order relation in equation (30). Indeed, the absence of symmetry planes due the irregularity of the pore arrangement means that the demonstration in subsection 3.3.2 does not apply to this type of microstructure.

One can thus conclude that for random periodic structures, the PBC result is unsurpassed by the MBC result, with the latter generally underestimating the ETC due to regions close to the

boundary not participating in heat transfer as they would in an infinite medium. The difference between the MBC and PBC results in the present case is however very slight.

5.3. Estimation of the effective thermal conductivity of reconstructed real foams

For the tomography-reconstructed real foam models, no rigorous numerical solution of the ETC can be obtained due to the non-periodic geometry. As such, the mean ATC of non-overlapping cubic subdomains of the reconstructed foam is used as an ETC estimate. Volumes between 0.0117 mm^3 and 11.5 mm^3 were considered, with the number of samples for each volume recorded in Table 3. To ensure statistical independence of the samples, care was taken such that the dimensions L of the smallest subdomains remain greater than the real foam's covariance range.

Volume V (mm^3)	0.0942	0.318	0.754	1.47	2.54	6.03	11.5
Number of samples	125	125	64	64	27	8	8
Porosity f_p (%)	74 ± 9	74 ± 5	74 ± 3	74 ± 2	74 ± 1	73.8 ± 0.5	74.0 ± 0.5

Table 3: Number of samples and porosity (stochastic mean and standard deviation) for each considered subdomain volume.

Near-diagonal mean ATC matrices were obtained in all cases, with an approximate difference of $\pm 6\%$ between eigenvalues. For the volumes considered, the variance between the ATC of different subdomains are much higher than that obtained with the periodic foams. Indeed, while the periodic foams all have the same porosity and only differ in terms of pore arrangement, the real foam subdomains considered here can have vastly different porosities, which is the main factor influencing the ATC. The variance of the ATC computed with the UTG, PBC and MBC decreases sharply with sample volume, in excellent agreement with the power law (34) proposed by Kanit et al. [20] (Figure 10). On the other hand, the UHF estimate has a relatively stable variance that is of several orders of magnitude smaller, showing an insensitivity towards pore volume fraction at high porosities.

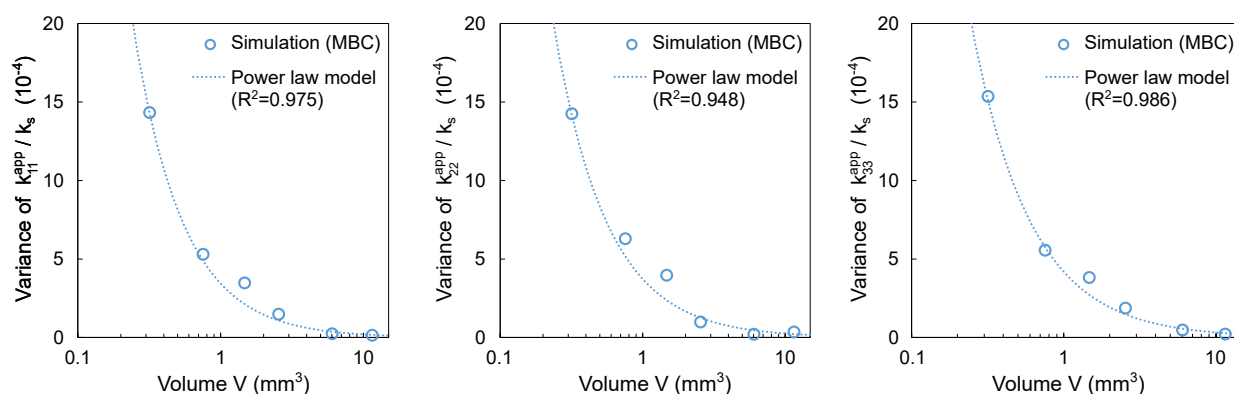


Figure 10: Variance of the normalized apparent thermal conductivity (ATC) of real foams of different volumes simulated with the mixed boundary conditions (MBC), with the power law fit proposed by Kanit et al. [20].

The integral range J_k and power law exponent α for the UTG, PBC and MBC identified from the numerical experiments are summarized in Table 4. The values of J_k confirm that the hypothesis

$V \gg J_k$ for equation (34) holds, and also $\alpha \approx 1$ in line with the findings of Kanit et al. [20]. The statistical RVE sizes ($V_{N=1}$ for a target precision $\epsilon_0 = 2\%$) estimated through equations (33) and (34) using the identified parameters are also given, showing notably that the ETC estimated with the MBC stabilizes at smaller volumes than with the PBC.

	J_k of k_{jj}^{app}/k_s (10^{-3} mm^3)			α of k_{jj}^{app}/k_s (-)			$V_{N=1}$ (mm^3)
	$j = 1$	$j = 2$	$j = 3$	$j = 1$	$j = 2$	$j = 3$	$\epsilon_0 = 2\%$
UTG	9.490	9.490	9.490	1.255	1.255	1.255	33
MBC	6.116	4.670	4.137	1.240	1.163	1.117	125
PBC	1.339	4.309	2.602	0.934	1.153	1.028	505

Table 4: Integral range J_k and power law exponent α corresponding to the diagonal terms of the normalized apparent thermal conductivity k_{app}/k_s of the real foam, under uniform temperature gradient (UTG), mixed (MBC) and periodic (PBC) boundary conditions. The size of the statistical representative volume element $V_{N=1}$ for a precision of $\epsilon_0 = 2\%$ was also given.

The mean and precision of the largest eigenvalue of the ATC obtained using different boundary conditions on subdomains of increasing volumes are shown in Figure 11. As with the results obtained on periodic foams, comparison was made with the series and parallel (Weiner) bounds, Maxwell-Eucken bounds, and the power law of Archie [47]. Once again, the UTG and UHF results are extremely far apart and thus uninformative. For every subdomain, the UTG systematically gives the parallel model result (upper Wiener bound); the narrow error bands observed simply reflect the slight variation in porosity—and thus the parallel model result—between individual subdomains. The MBC results are slightly more precise than the PBC results, both in absolute and relative terms.

The estimate given by the PBC is now systematically and significantly inferior to the MBC result, in agreement with the order relation $k_{\text{app}}^{\text{PBC}} \leq k_{\text{app}}^{\text{MBC}}$ (30) demonstrated in subsection 3.3.2. While no rigorous reference ETC value exists, one can nonetheless see that the ETC estimated under the PBC slowly tends towards the MBC result (instead of the other way round), suggesting that the converged value is closer to the MBC result than it is to the PBC result. Coupled with the results from the preliminary study on unit cell-based geometries (see subsection 5.1), this observation gives strong evidence that the MBC give more accurate estimates of the ETC than the PBC for non-periodic foam microstructures.

5.4. Verification of theoretical postulates

In the next subsections, the postulates in section 3 are verified with the results of the numerical case studies. Notably, the validity of the mixed boundary conditions (MBC) for statistically homogeneous foams and the order relation between the apparent thermal conductivities (ATC) computed under the MBC and periodic boundary conditions (PBC) are examined.

5.4.1. Macrohomogeneity condition and validity of the mixed boundary conditions

For all the considered cases, the entropy residual r_s (31) was systematically checked to ensure that the macrohomogeneity condition is satisfied. Figure 12 shows, for the tomography-reconstructed real foams, the evolution of the mean entropy residual with sample volume for

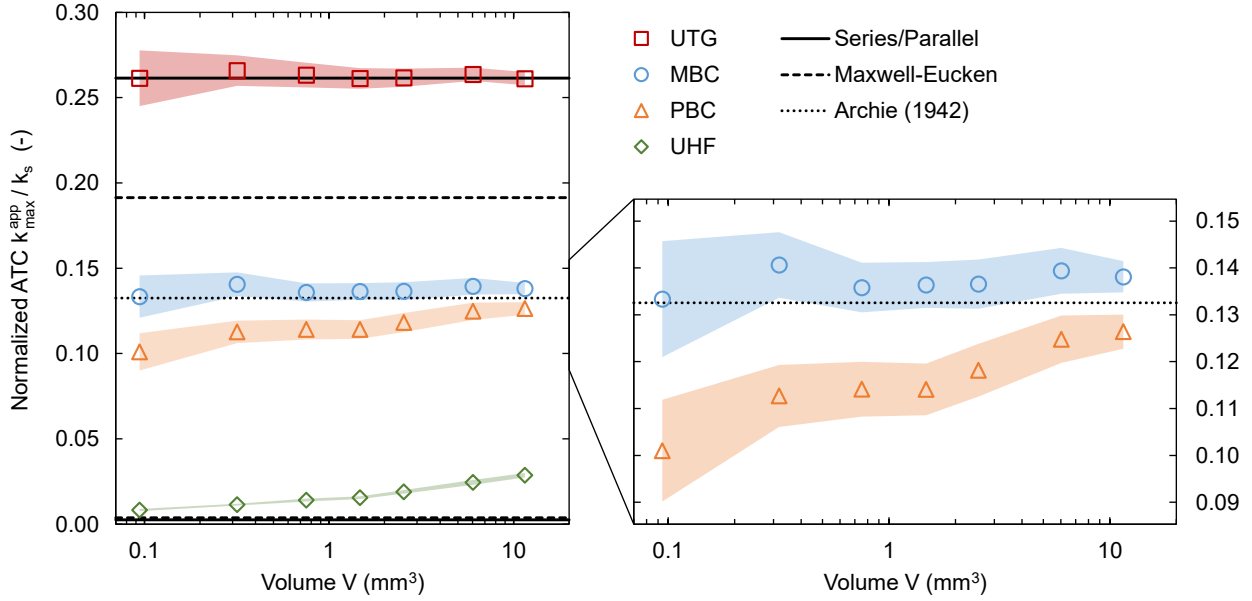


Figure 11: Mean normalized apparent thermal conductivity (ATC) of non-periodic real foam samples of increasing volume, under uniform heat flux (UHF), uniform temperature gradient (UTG), periodic (PBC) and mixed (MBC) boundary conditions. Comparison was shown for the largest eigenvalue of the ATC. The error bands indicate the standard error.

different boundary conditions. The uniform temperature gradient (UTG) boundary conditions systematically gave a residual of exactly 0% showing that the macrohomogeneity condition was perfectly satisfied. However, a low, non-zero residual was found for the other cases, most likely due to the use of a “displacement-based” finite element solver [45] which introduces small discretization errors where exact temperature boundary conditions are not given.

At large domain sizes, the low residual ($r_s < 1\%$) shows that all the considered boundary conditions satisfy the macrohomogeneity condition. At small domain sizes, the residual obtained with the MBC rises sharply with a much larger scatter (compared to that obtained with the PBC, which only rises slightly due to the increased discretization error). This observation certainly supports the postulate made in subsection 3.2.2: that the MBC satisfy the sufficient condition for macrohomogeneity (21) as long the sample contains a statistically homogeneous spatial distribution of pores, since a smaller foam volume with respect to the characteristic pore size would imply a less homogeneous spatial distribution of pores within the sample. To illustrate this, the normalized temperature difference between opposite lateral faces ($\partial\Omega_3$) is compared in Figure 13 for two different volumes: the smaller sample ($V = 0.318 \text{ mm}^3$, $L/\ell \approx 1.9$) has significantly larger differences between the temperature fields on opposite faces compared to the larger sample ($V = 2.54 \text{ mm}^3$, $L/\ell \approx 3.9$) for which the difference is close to zero.

5.4.2. Comparison of the apparent conductivities of non-periodic foams under periodic and mixed boundary conditions

In subsection 3.3.2, the order relation $k_{\text{app}}^{\text{PBC}} \leq k_{\text{app}}^{\text{MBC}}$ (28) was demonstrated with the postulate that the boundary normal heat flux under the PBC vanishes on the lateral faces for non-periodic

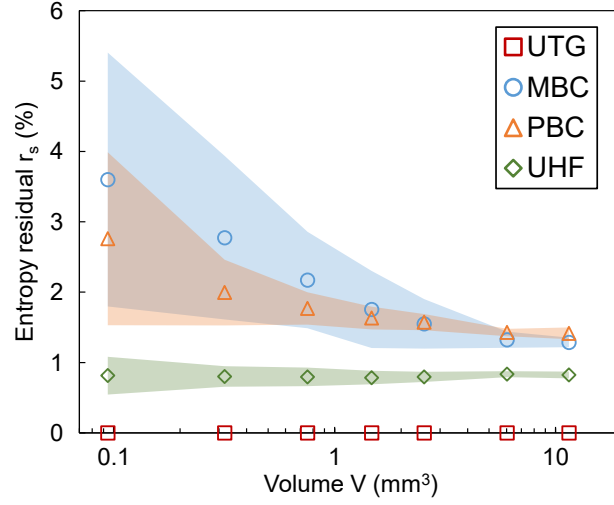


Figure 12: Mean entropy residual r_s as a function of real foam volume under uniform heat flux (UHF), uniform temperature gradient (UTG), periodic (PBC) and mixed (MBC) boundary conditions. The error bars indicate the standard deviation.

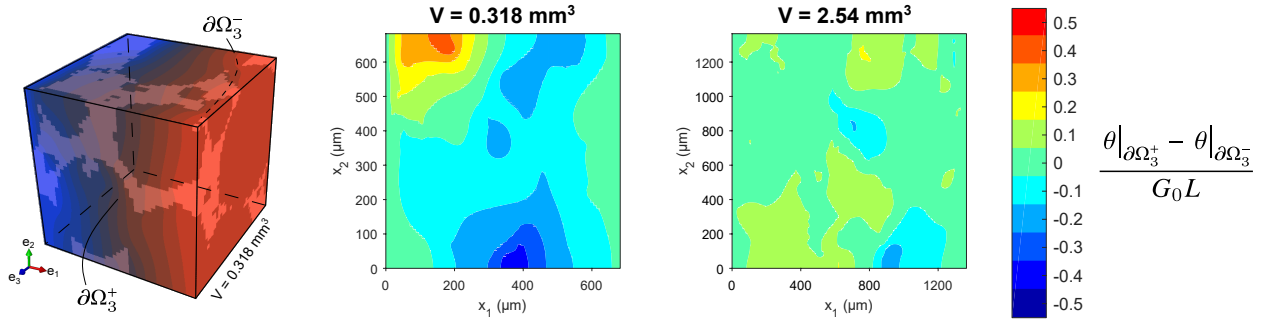


Figure 13: Normalized temperature difference on opposite pairs of lateral $\partial\Omega_3$ faces of non-periodic real foams of different volumes subjected to the mixed boundary conditions (MBC).

foams of high porosity, due to a combination of high phase contrast and high geometrical mismatch.

Figure 14 illustrates the normal heat flux q_n on the boundaries of a non-periodic real foam model subjected to the PBC, and compares it with the geometrical features on the corresponding boundaries: for each pair of opposite boundary faces, the white regions show regions at which the solid phase is present on both faces, the black regions show regions at which the pore phase is present on both faces, and the gray regions indicate regions with boundary geometry mismatch.

One sees that q_n^{PBC} is indeed non-zero on the boundaries only where the solid phase is present on both sides. While high values of q_n^{PBC} are seen on the $\partial\Omega_1$ faces perpendicular to the imposed temperature gradient, low values close to zero are generally seen on the lateral faces even when there is “continuity” of the solid phase across opposite lateral faces. This observation supports the postulate that the combined effect of geometrical mismatch on the lateral faces and high phase contrast reduces q_n^{PBC} to zero on lateral faces, confirming the theoretical status of the demonstrated order relation $k_{\text{app}}^{\text{PBC}} \leq k_{\text{app}}^{\text{MBC}}$ for non-periodic, highly porous foams.

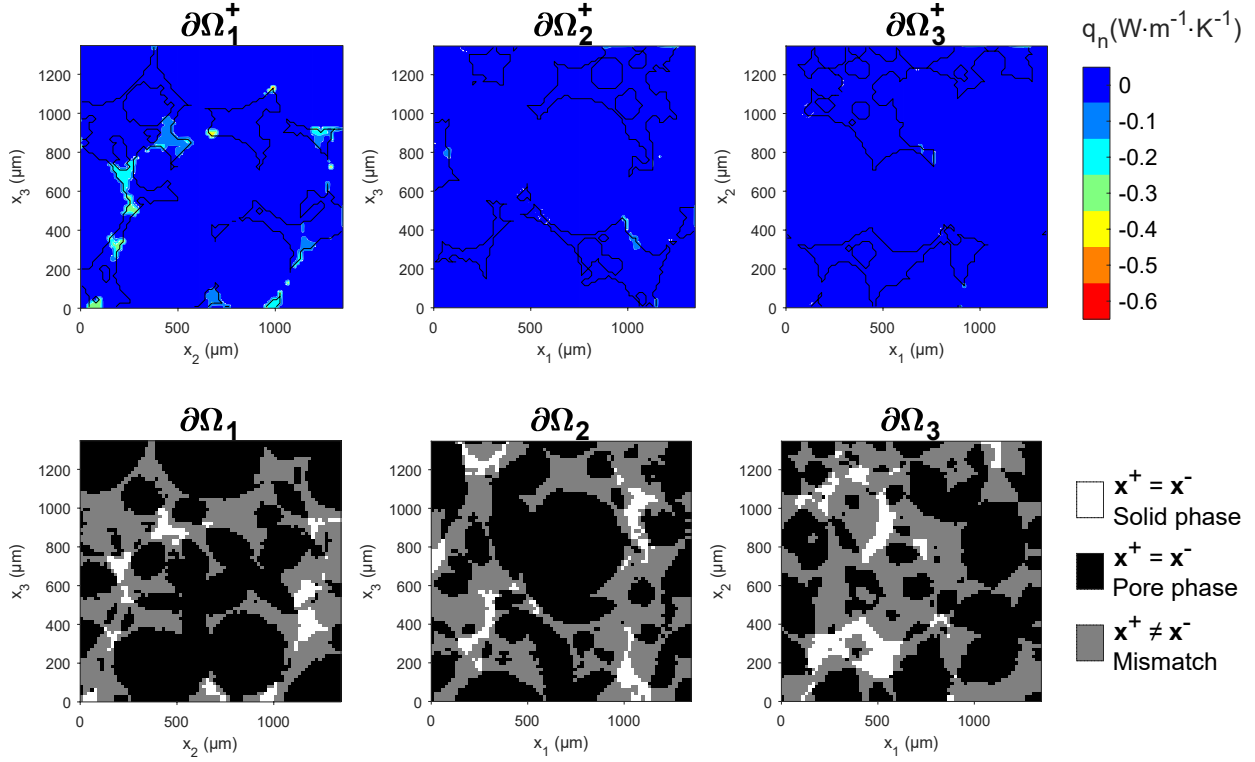


Figure 14: Comparison of the normal heat flux obtained using periodic boundary conditions (PBC) on a real foam of $V = 2.54 \text{ mm}^3$, and the geometry mismatch on pairs of opposite faces (white: solid phase on both sides; black: pore phase on both sides; gray: different phases on both sides).

6. Conclusion

In performing computational homogenization on microstructures smaller than the representative volume element (RVE), the apparent thermal conductivity (ATC) under different boundary conditions are generally biased estimates of the effective thermal conductivity (ETC) of the entire medium due to edge effects. The present theoretical and numerical study clarified the influence of boundary conditions on the validity, precision and accuracy of the ETC thus estimated for open-cell foams of sub-RVE sizes with porosities close to 74%. Three different types of foam models were considered: unit cell-based structures, digitally generated periodic foams, and tomography-reconstructed real foams. When the microstructure is random, the resulting scatter in the ATC is taken into account by averaging over several equivalent samples, and a statistical treatment proposed by Kanit et al. [20] based on the integral range was used to estimate the confidence interval, as well as the statistical RVE size associated with a given precision.

Due to the high porosity of the considered microstructures and the high contrast between the thermal conductivities of the solid and pore phases, an extremely wide gap was observed between the numerical lower and upper bounds given by the uniform heat flux (UHF) and uniform temperature gradient (UTG) boundary conditions respectively. The extremely slow convergence of these two bounds is evidence of the prohibitively large RVE size, and renders these boundary conditions impractical for estimating the ETC of foams. The UTG result can be particularly misleading as it

systematically gives an isotropic ATC equal to the parallel model result (upper Wiener bound) for the considered computational volumes, even when significant orthotropy exists.

The set of mixed boundary conditions (MBC) considered in this work was shown to satisfy the macrohomogeneity condition for foam samples in which the pores are distributed homogeneously, and thus provide thermodynamically valid ETC estimates under the homogenization framework. While this rule of thumb may be used to determine *a priori* the types of microstructures on which the MBC can be used, it is still recommended to verify this point on a case-by-case basis (i.e., by computing the entropy residual r_S defined in equation (31)).

Contrary to the common view that periodic boundary conditions (PBC) give the best possible estimate of the ETC for any given microstructure, for non-periodic foam microstructures, the aforementioned MBC are shown to provide more accurate and precise ETC estimates. Indeed, the PBC significantly underestimate the ETC under the combined effect of high phase contrast and high geometrical mismatch on the lateral boundaries.

The reverse is true for periodic foams with irregular porosity: while the PBC directly give the reference ETC value, the MBC lead to an underestimation of the ETC, although in the present investigation, the confidence intervals of both results lay very close. Identical results are obtained for the MBC and PBC results for periodic structures in which symmetry planes exist for the geometry (e.g., the regular isotropic unit cells studied by [24]).

The guidelines established in this work should improve the accuracy and precision of foam microstructure-property relations predicted through direct pore-scale modeling. Future work could focus on numerical modeling on gigantic samples (using more appropriate alternatives such as FFT-based techniques [48, 49]) to attempt to reproduce the present results for foam sizes close to or exceeding the RVE. Also of interest is the development of more realistic, physics-based periodic foam generation techniques, which may eliminate the need for costly direct computation on tomography-reconstructed foam samples without sacrificing the accuracy of the morphological description and hence the estimated ETC. While the present study focuses on thermal conduction modeling in foams, extensions to other physical phenomena such as permeability, elasticity, and plasticity (with appropriate treatments to handle nonlinear behavior [16, 50]) are most certainly of interest for future investigations.

7. Acknowledgments

This research was supported by Saint-Gobain Research (SGR) Provence and the French National Association for Research and Technology (ANRT) through the CIFRE grant number 2017/0775. The authors would like to express their gratitude to L. San Miguel (SGR Provence), L. Pierrot (SGR Provence) and J. Meulemans (SGR Paris) for their insight and discussions that greatly assisted the research, to Y. Millot (SGR Provence) for the preparation of foam samples, and to J. Adrien (MATEIS laboratory) for assistance with X-ray tomography.

Appendix A. Mean field computation for different boundary value problems

For a volume Ω with boundary $\partial\Omega$ on which a differentiable scalar field ψ and a vector field Ψ are defined, the divergence theorem and its corollary state that:

$$\int_{\Omega} \nabla \cdot \Psi \, dV = \int_{\partial\Omega} \Psi \cdot \mathbf{n} \, dA \quad (\text{A.1a})$$

$$\int_{\Omega} \nabla \psi \, dV = \int_{\partial\Omega} \psi \mathbf{n} \, dA \quad (\text{A.1b})$$

The heat flux \mathbf{q} can be expanded using the relations $\nabla \mathbf{x} = \mathbf{I}$ (the identity tensor) and $\nabla \cdot \mathbf{q} = 0$:

$$\mathbf{q} = \mathbf{q} \cdot \nabla \mathbf{x} = \nabla \cdot (\mathbf{q}\mathbf{x}) - (\nabla \cdot \mathbf{q})\mathbf{x} \quad (\text{A.2})$$

The mean heat flux $\langle \mathbf{q} \rangle$ is then written as a boundary integral:

$$\begin{aligned} \langle \mathbf{q} \rangle &= \frac{1}{V} \int_{\Omega} \mathbf{q} \, dV = \frac{1}{V} \int_{\Omega} \nabla \cdot (\mathbf{q}\mathbf{x}) \, dV \\ &= \frac{1}{V} \int_{\partial\Omega} (\mathbf{q}\mathbf{x}) \cdot \mathbf{n} \, dA = \frac{1}{V} \int_{\partial\Omega} q_n \mathbf{x} \, dA \end{aligned} \quad (\text{A.3})$$

Rewriting the mean temperature gradient $\langle \nabla \theta \rangle$ as a boundary integral requires simple application of the divergence theorem (A.1):

$$\langle \nabla \theta \rangle = \frac{1}{V} \int_{\Omega} \nabla \theta \, dV = \frac{1}{V} \int_{\partial\Omega} \theta \mathbf{n} \, dA \quad (\text{A.4})$$

As for the mean specific entropy production rate $\langle \mathbf{q} \cdot \nabla \theta \rangle$, a similar development as in equation (A.3) is undertaken:

$$\begin{aligned} \langle \mathbf{q} \cdot \nabla \theta \rangle &= \frac{1}{V} \int_{\Omega} \mathbf{q} \cdot \nabla \theta \, dV = \frac{1}{V} \int_{\Omega} \nabla \cdot (\mathbf{q}\theta) \, dV \\ &= \frac{1}{V} \int_{\partial\Omega} (\mathbf{q}\theta) \cdot \mathbf{n} \, dA = \frac{1}{V} \int_{\partial\Omega} q_n \theta \, dA \end{aligned} \quad (\text{A.5})$$

Equations (A.3) to (A.5) are then applied to each boundary condition to demonstrate their validity with respect to the macrohomogeneity condition, as shown below.

Uniform heat flux (UHF). Using equation (12) as a starting point, the macroscopic heat flux $\mathbf{F} = \langle \mathbf{q} \rangle$ is computed:

$$\mathbf{F} = \frac{1}{V} \int_{\partial\Omega} \mathbf{x} (\mathbf{F}_0 \cdot \mathbf{n}) \, dA = \frac{1}{V} \int_{\Omega} \mathbf{F}_0 \, dV = \mathbf{F}_0 \quad (\text{A.6})$$

From relation (A.5), it can then be shown that the macrohomogeneity condition in (11) is automatically satisfied:

$$\langle \mathbf{q} \cdot \nabla \theta \rangle = \frac{1}{V} \int_{\partial\Omega} (\mathbf{F}_0 \cdot \mathbf{n}) \theta \, dA = \mathbf{F}_0 \cdot \left(\frac{1}{V} \int_{\partial\Omega} \theta \mathbf{n} \, dA \right) = \langle \mathbf{q} \rangle \cdot \langle \nabla \theta \rangle \quad (\text{A.7})$$

Uniform temperature gradient (UTG). Using equation (13) as a starting point, the macroscopic temperature gradient $\mathbf{G} = \langle \nabla \theta \rangle$ can be computed (knowing that $\nabla \mathbf{x} = \mathbf{I}$ the identity tensor):

$$\mathbf{G} = \frac{1}{V} \int_{\Omega} \nabla(\mathbf{G}_0 \cdot \mathbf{x}) dV = \frac{1}{V} \int_{\Omega} \mathbf{G}_0 \cdot (\nabla \mathbf{x}) dV = \mathbf{G}_0 \quad (\text{A.8})$$

The macrohomogeneity condition in (11) is also automatically satisfied:

$$\langle \mathbf{q} \cdot \nabla \theta \rangle = \frac{1}{V} \int_{\partial \Omega} q_n(\mathbf{G}_0 \cdot \mathbf{x}) dA = \left(\frac{1}{V} \int_{\partial \Omega} q_n \mathbf{x} dA \right) \cdot \mathbf{G}_0 = \langle \mathbf{q} \rangle \cdot \langle \nabla \theta \rangle \quad (\text{A.9})$$

Periodic boundary conditions (PBC). The temperature field over the domain is split as follows:

$$\forall \mathbf{x} \in \Omega, \quad \theta = \mathbf{G}_0 \cdot \mathbf{x} + \tilde{\theta} \quad (\text{A.10})$$

where $\tilde{\theta}$ is the fluctuation due to the micro-scale heterogeneities. The periodicity of $\tilde{\theta}$ is imposed in the PBC, as shown by rewriting equation (14):

$$\forall \mathbf{x} \in \partial \Omega, \quad \tilde{\theta}(\mathbf{x}^+) = \theta(\mathbf{x}^+) - \mathbf{G}_0 \cdot \mathbf{x}^+ = \theta(\mathbf{x}^-) - \mathbf{G}_0 \cdot \mathbf{x}^- = \tilde{\theta}(\mathbf{x}^-) \quad (\text{A.11})$$

In the expression of the macroscopic temperature gradient $\mathbf{G} = \langle \nabla \theta \rangle$, the boundary integral involving $\tilde{\theta}$ vanishes due to its periodicity:

$$\mathbf{G} = \frac{1}{V} \left(\int_{\Omega} \nabla(\mathbf{G}_0 \cdot \mathbf{x}) dV + \int_{\partial \Omega} \tilde{\theta} \mathbf{n} dA \right) = \mathbf{G}_0 \quad (\text{A.12})$$

In a similar fashion, knowing that q_n is anti-periodic, the term involving $\tilde{\theta}$ in $\langle \mathbf{q} \cdot \nabla \theta \rangle$ also vanishes, and the macrohomogeneity condition in (11) is satisfied:

$$\langle \mathbf{q} \cdot \nabla \theta \rangle = \frac{1}{V} \left(\int_{\partial \Omega} q_n(\mathbf{G}_0 \cdot \mathbf{x}) dA + \int_{\partial \Omega} q_n \tilde{\theta} dA \right) = \langle \mathbf{q} \rangle \cdot \langle \nabla \theta \rangle \quad (\text{A.13})$$

Mixed boundary conditions (MBC). The mean fields are directly obtained from the application of equations (A.3)–(A.5), replacing with the boundary conditions in (15).

Appendix B. Proofs of known order relations between the ATC computed with different boundary conditions

Result #1. Comparison of the PBC and UTG results ($\mathbf{k}_{\text{app}}^{\text{PBC}} \leq \mathbf{k}_{\text{app}}^{\text{UTG}}$) in equation (25):

$$S^{\text{UTG}}(\mathbf{q}^{\text{PBC}}) \leq S^{\text{UTG}}(\mathbf{q}^{\text{UTG}}) \iff \left(\mathbf{k}_{\text{app}}^{\text{PBC}} \cdot \mathbf{G}_0 \right) \cdot \mathbf{G}_0 \leq \left(\mathbf{k}_{\text{app}}^{\text{UTG}} \cdot \mathbf{G}_0 \right) \cdot \mathbf{G}_0 \quad (\text{B.1})$$

Proof #1. The right hand side expands as follows:

$$\mathcal{S}^{\text{UTG}}(\mathbf{q}^{\text{UTG}}) = -\mathcal{S}_c^{\text{UTG}}(\theta^{\text{UTG}}) = \left(\mathbf{k}_{\text{app}}^{\text{UTG}} \cdot \langle \nabla \theta \rangle^{\text{UTG}} \right) \cdot \langle \nabla \theta \rangle^{\text{UTG}} = \left(\mathbf{k}_{\text{app}}^{\text{UTG}} \cdot \mathbf{G}_0 \right) \cdot \mathbf{G}_0 \quad (\text{B.2})$$

The left hand side expands as follows:

$$\begin{aligned} \mathcal{S}^{\text{UTG}}(\mathbf{q}^{\text{PBC}}) &= - \int_{\partial\Omega} (\mathbf{q}^{\text{PBC}} \cdot \mathbf{n}) \theta^{\text{UTG}} \, dA - \frac{V}{2} \langle \mathbf{q} \rangle^{\text{PBC}} \cdot \left((\mathbf{k}_{\text{app}}^{\text{PBC}})^{-1} \cdot \langle \mathbf{q} \rangle^{\text{PBC}} \right) \\ &= - \int_{\partial\Omega} (\mathbf{q}^{\text{PBC}} \cdot \mathbf{n}) (\mathbf{G}_0 \cdot \mathbf{x}) \, dA - \frac{V}{2} \langle \mathbf{q} \rangle^{\text{PBC}} \cdot \mathbf{G}_0 \\ &= -V \langle \mathbf{q} \rangle^{\text{PBC}} \cdot \mathbf{G}_0 + \frac{V}{2} \langle \mathbf{q} \rangle^{\text{PBC}} \cdot \mathbf{G}_0 \\ &= \left(\mathbf{k}_{\text{app}}^{\text{PBC}} \cdot \mathbf{G}_0 \right) \cdot \mathbf{G}_0 \end{aligned} \quad (\text{B.3})$$

Result #2. Comparison of the PBC and UHF results ($\mathbf{k}_{\text{app}}^{\text{UHF}} \leq \mathbf{k}_{\text{app}}^{\text{PBC}}$) in equation (25):

$$\mathcal{S}_c^{\text{UHF}}(\theta^{\text{PBC}}) \leq \mathcal{S}_c^{\text{UHF}}(\theta^{\text{UHF}}) \iff \frac{V}{2} \mathbf{F}_0 \cdot \left((\mathbf{k}_{\text{app}}^{\text{PBC}})^{-1} \cdot \mathbf{F}_0 \right) \leq \frac{V}{2} \mathbf{F}_0 \cdot \left((\mathbf{k}_{\text{app}}^{\text{UHF}})^{-1} \cdot \mathbf{F}_0 \right) \quad (\text{B.4})$$

Proof #2. The right hand side expands as follows:

$$\mathcal{S}_c^{\text{UHF}}(\theta^{\text{UHF}}) = -\mathcal{S}^{\text{UHF}}(\mathbf{q}^{\text{UHF}}) = \frac{V}{2} \langle \mathbf{q} \rangle^{\text{UHF}} \cdot \left((\mathbf{k}_{\text{app}}^{\text{UHF}})^{-1} \cdot \langle \mathbf{q} \rangle^{\text{UHF}} \right) = \frac{V}{2} \mathbf{F}_0 \cdot \left((\mathbf{k}_{\text{app}}^{\text{UHF}})^{-1} \cdot \mathbf{F}_0 \right) \quad (\text{B.5})$$

The left hand side expands as follows:

$$\begin{aligned} \mathcal{S}_c^{\text{UHF}}(\theta^{\text{PBC}}) &= - \int_{\partial\Omega} (\mathbf{q}^{\text{UHF}} \cdot \mathbf{n}) \theta^{\text{PBC}} \, dA - \frac{V}{2} \left(\mathbf{k}_{\text{app}}^{\text{PBC}} \cdot \langle \nabla \theta \rangle^{\text{PBC}} \right) \cdot \langle \nabla \theta \rangle^{\text{PBC}} \\ &= - \int_{\partial\Omega} (\mathbf{F}_0 \cdot \mathbf{n}) \theta^{\text{PBC}} \, dA - \frac{V}{2} \langle \mathbf{q} \rangle^{\text{PBC}} \cdot \langle \nabla \theta \rangle^{\text{PBC}} \\ &= -V \mathbf{F}_0 \cdot \langle \nabla \theta \rangle^{\text{PBC}} - \frac{V}{2} \langle \mathbf{q} \rangle^{\text{PBC}} \cdot \langle \nabla \theta \rangle^{\text{PBC}} \\ &= V \mathbf{F}_0 \cdot \left((\mathbf{k}_{\text{app}}^{\text{PBC}})^{-1} \cdot \langle \mathbf{q} \rangle^{\text{PBC}} \right) - \frac{V}{2} \langle \mathbf{q} \rangle^{\text{PBC}} \cdot \left((\mathbf{k}_{\text{app}}^{\text{PBC}})^{-1} \cdot \langle \mathbf{q} \rangle^{\text{PBC}} \right) \equiv \Pi_c \left(\langle \mathbf{q} \rangle^{\text{PBC}} \right) \end{aligned} \quad (\text{B.6})$$

Setting $\Pi_c(\langle \mathbf{q} \rangle^{\text{PBC}})$ to represent the expression on the last line, one can then deduce:

$$\begin{cases} \left. \frac{\partial \Pi_c}{\partial \langle \mathbf{q} \rangle^{\text{PBC}}} \right|_{\langle \mathbf{q} \rangle^{\text{PBC}} = \mathbf{F}_0} = V \mathbf{F}_0 \cdot (\mathbf{k}_{\text{app}}^{\text{PBC}})^{-1} - V \langle \mathbf{q} \rangle^{\text{PBC}} \cdot (\mathbf{k}_{\text{app}}^{\text{PBC}})^{-1} = \mathbf{0} \\ \frac{\partial^2 \Pi_c}{(\partial \langle \mathbf{q} \rangle^{\text{PBC}})^2} = -V (\mathbf{k}_{\text{app}}^{\text{PBC}})^{-1} \leq \mathbf{0} \quad \forall \langle \mathbf{q} \rangle^{\text{PBC}} \end{cases} \quad (\text{B.7})$$

$$\iff \max \mathcal{S}_c^{\text{UHF}}(\theta^{\text{PBC}}) = \max \Pi_c \left(\langle \mathbf{q} \rangle^{\text{PBC}} \right) = \Pi_c(\mathbf{F}_0) = \frac{V}{2} \mathbf{F}_0 \cdot \left((\mathbf{k}_{\text{app}}^{\text{PBC}})^{-1} \cdot \mathbf{F}_0 \right)$$

Result #3. Comparison of the MBC and UTG results ($\mathbf{k}_{\text{app}}^{\text{MBC}} \leq \mathbf{k}_{\text{app}}^{\text{UTG}}$) in equation (26) according to the work of Hazanov and Huet [42]:

$$\mathcal{S}^{\text{UTG}}(\mathbf{q}^{\text{MBC}}) \leq \mathcal{S}^{\text{UTG}}(\mathbf{q}^{\text{UTG}}) \iff \frac{V}{2}(\mathbf{k}_{\text{app}}^{\text{MBC}} \cdot \mathbf{G}_0) \cdot \mathbf{G}_0 \leq \frac{V}{2}(\mathbf{k}_{\text{app}}^{\text{UTG}} \cdot \mathbf{G}_0) \cdot \mathbf{G}_0 \quad (\text{B.8})$$

Proof #3. The right hand side expands as follows:

$$\mathcal{S}^{\text{UTG}}(\mathbf{q}^{\text{UTG}}) = -\mathcal{S}_c^{\text{UTG}}(\theta^{\text{UTG}}) = \frac{V}{2}(\mathbf{k}_{\text{app}}^{\text{UTG}} \cdot \langle \nabla \theta \rangle^{\text{UTG}}) \cdot \langle \nabla \theta \rangle^{\text{UTG}} = \frac{V}{2}(\mathbf{k}_{\text{app}}^{\text{UTG}} \cdot \mathbf{G}_0) \cdot \mathbf{G}_0 \quad (\text{B.9})$$

The left hand side expands as follows:

$$\begin{aligned} \mathcal{S}^{\text{UTG}}(\mathbf{q}^{\text{MBC}}) &= - \int_{\partial\Omega} (\mathbf{q}^{\text{MBC}} \cdot \mathbf{n}) \theta^{\text{UTG}} \, dA - \frac{V}{2} \langle \mathbf{q} \rangle^{\text{MBC}} \cdot \left((\mathbf{k}_{\text{app}}^{\text{MBC}})^{-1} \cdot \langle \mathbf{q} \rangle^{\text{MBC}} \right) \\ &= - \int_{\partial\Omega} (\mathbf{q}^{\text{MBC}} \cdot \mathbf{n})(\mathbf{G}_0 \cdot \mathbf{x}) \, dA - \frac{V}{2} \langle \mathbf{q} \rangle^{\text{MBC}} \cdot \left((\mathbf{k}_{\text{app}}^{\text{MBC}})^{-1} \cdot \langle \mathbf{q} \rangle^{\text{MBC}} \right) \\ &= -V \langle \mathbf{q} \rangle^{\text{MBC}} \cdot \mathbf{G}_0 - \frac{V}{2} \langle \mathbf{q} \rangle^{\text{MBC}} \cdot \left((\mathbf{k}_{\text{app}}^{\text{MBC}})^{-1} \cdot \langle \mathbf{q} \rangle^{\text{MBC}} \right) \equiv \Pi(\langle \mathbf{q} \rangle^{\text{MBC}}) \end{aligned} \quad (\text{B.10})$$

Setting $\Pi(\langle \mathbf{q} \rangle^{\text{MBC}})$ to represent the expression the last line, one can then deduce:

$$\begin{cases} \left. \frac{\partial \Pi}{\partial \langle \mathbf{q} \rangle^{\text{MBC}}} \right|_{\langle \mathbf{q} \rangle^{\text{MBC}} = -\mathbf{k}_{\text{app}}^{\text{MBC}} \cdot \mathbf{G}_0} = -V \mathbf{G}_0 - V (\mathbf{k}_{\text{app}}^{\text{MBC}})^{-1} \cdot \langle \mathbf{q} \rangle^{\text{MBC}} = \mathbf{0} \\ \frac{\partial^2 \Pi}{(\partial \langle \mathbf{q} \rangle^{\text{MBC}})^2} = -V (\mathbf{k}_{\text{app}}^{\text{MBC}})^{-1} \leq \mathbf{0} \quad \forall \langle \mathbf{q} \rangle^{\text{MBC}} \end{cases} \quad (\text{B.11})$$

$$\iff \max \mathcal{S}^{\text{UTG}}(\mathbf{q}^{\text{MBC}}) = \max \Pi(\langle \mathbf{q} \rangle^{\text{MBC}}) = \Pi(-\mathbf{k}_{\text{app}}^{\text{MBC}} \cdot \mathbf{G}_0) = \frac{V}{2}(\mathbf{k}_{\text{app}}^{\text{MBC}} \cdot \mathbf{G}_0) \cdot \mathbf{G}_0$$

The comparison of the MBC and UHF results ($\mathbf{k}_{\text{app}}^{\text{UHF}} \leq \mathbf{k}_{\text{app}}^{\text{MBC}}$) in equation (26) can be demonstrated in the exact same manner as for result #2, by replacing all occurrences of ‘PBC’ with ‘MBC’ in equations (B.4), (B.6) and (B.7).

Data availability

The raw and processed data in this work cannot be made publicly available at this time as they are part of an ongoing study.

References

- [1] S. Suter, A. Steinfeld, S. Haussener, Pore-level engineering of macroporous media for increased performance of solar-driven thermochemical fuel processing, *International Journal of Heat and Mass Transfer* 78 (2014) 688–698.
- [2] J. Petrasch, B. Schrader, P. Wyss, A. Steinfeld, Tomography-based determination of the effective thermal conductivity of fluid-saturated reticulate porous ceramics, *Journal of Heat Transfer* 130 (2008) 032602.

- [3] D. Baillis, R. Coquard, J. Randrianalisoa, L. A. Dombrovsky, R. Viskanta, Thermal Radiation Properties of Highly Porous Cellular Foams, *Special Topics & Reviews in Porous Media - An International Journal* 4 (2013) 111–136.
- [4] W. Zhu, N. Blal, S. Cunsolo, D. Baillis, Micromechanical modeling of effective elastic properties of open-cell foam, *International Journal of Solids and Structures* 115-116 (2017) 61–72.
- [5] M. Schumann, L. San Miguel, Fiber-Free Ceramic Insulation Foam for Highest Temperatures – a New Generation of HSE-friendly Refractory Products with Multiple Application Possibilities, *refractories WORLDFORUM* 9 (2017) 50–58.
- [6] W. Pabst, E. Gregorová, Conductivity of porous materials with spheroidal pores, *Journal of the European Ceramic Society* 34 (2014) 2757–2766.
- [7] P. Ranut, On the effective thermal conductivity of aluminum metal foams: Review and improvement of the available empirical and analytical models, *Applied Thermal Engineering* 101 (2016) 496–524.
- [8] P. Kumar, F. Topin, J. Vicente, Determination of effective thermal conductivity from geometrical properties: Application to open cell foams, *International Journal of Thermal Sciences* 81 (2014) 13–28.
- [9] D. Baillis, R. Coquard, S. Cunsolo, Effective conductivity of Voronoi’s closed- and open-cell foams: analytical laws and numerical results, *Journal of Materials Science* 52 (2017) 11146–11167.
- [10] S. Cunsolo, D. Baillis, N. Bianco, Improved Monte Carlo methods for computational modelling of thermal radiation applied to porous cellular materials, *International Journal of Thermal Sciences* 137 (2019) 161–179.
- [11] W. Tian, L. Qi, X. Chao, J. Liang, M. Fu, Numerical evaluation on the effective thermal conductivity of the composites with discontinuous inclusions: Periodic boundary condition and its numerical algorithm, *International Journal of Heat and Mass Transfer* 134 (2019) 735–751.
- [12] R. Coquard, D. Rochais, D. Baillis, Modeling of the Coupled Conductive and Radiative Heat Transfer in Nicalor From Photothermal Measurements and X-Ray Tomography, *Special Topics & Reviews in Porous Media - An International Journal* 2 (2011) 249–265.
- [13] M. A. Mendes, S. Ray, D. Trimis, A simple and efficient method for the evaluation of effective thermal conductivity of open-cell foam-like structures, *International Journal of Heat and Mass Transfer* 66 (2013) 412–422.
- [14] J. Lux, A. Ahmadi, C. Gobbe, C. Delis e, Macroscopic thermal properties of real fibrous materials: Volume averaging method and 3D image analysis, *International Journal of Heat and Mass Transfer* 49 (2006) 1958–1973.
- [15] F. Panerai, J. C. Ferguson, J. Lachaud, A. Martin, M. J. Gasch, N. N. Mansour, Micro-tomography based analysis of thermal conductivity, diffusivity and oxidation behavior of rigid and flexible fibrous insulators, *International Journal of Heat and Mass Transfer* 108 (2017) 801–811.
- [16] M. G. Geers, V. G. Kouznetsova, W. A. Brekelmans, Multi-scale computational homogenization: Trends and challenges, *Journal of Computational and Applied Mathematics* 234 (2010) 2175–2182.
- [17] J.-C. Michel, H. Moulinec, P. Suquet, Composites   microstructure p riodique [Composites with periodic microstructures], in: M. Bornert, T. Bretheau, P. Gilormini (Eds.), *Homog enisation en m canique des mat riaux 1. Mat riaux al atoires  lastiques et milieux p riodiques*, HERMES Science Europe Ltd, Paris, France, 2001, pp. 57–92.
- [18] J. Qu, M. Cherkaoui, *Fundamentals of Micromechanics of Solids*, John Wiley & Sons, Inc, 2006.
- [19] I.  zdemir, W. A. M. Brekelmans, M. G. D. Geers, Computational homogenization for heat conduction in heterogeneous solids, *International Journal for Numerical Methods in Engineering* 73 (2008) 185–204.
- [20] T. Kanit, S. Forest, I. Galliet, V. Mounoury, D. Jeulin, Determination of the size of the representative volume element for random composites: Statistical and numerical approach, *International Journal of Solids and Structures* 40 (2003) 3647–3679.
- [21] J. Dirrenberger, S. Forest, D. Jeulin, Towards gigantic RVE sizes for 3D stochastic fibrous networks, *International Journal of Solids and Structures* 51 (2014) 359–376.
- [22] R. Hill, Elastic properties of reinforced solids: Some theoretical principles, *Journal of the Mechanics and Physics of Solids* 11 (1963) 357–372.
- [23] S. Schindler, J. Mergheim, M. Zimmermann, J. C. Aurich, P. Steinmann, Numerical homogenization of elastic and thermal material properties for metal matrix composites (MMC), *Continuum Mechanics and Thermodynamics* 29 (2017) 51–75.

- [24] M. Jiang, I. Jasiuk, M. Ostoja-Starzewski, Apparent thermal conductivity of periodic two-dimensional composites, *Computational Materials Science* 25 (2002) 329–338.
- [25] A. Bensoussan, J.-L. Lions, G. Papanicolaou, Asymptotic Analysis for Periodic Structures, in: J.-L. Lions, G. Papanicolaou, R. Rockafellar (Eds.), *Studies in Mathematics and its Applications*, volume 5, North-Holland Publishing Company, Amsterdam, 1978, pp. 1–700. doi:10.1016/S0168-2024(08)70194-2.
- [26] E. Sanchez-Palencia, Non-Homogeneous Media and Vibration Theory, volume 127 of *Lecture Notes in Physics*, Springer Berlin Heidelberg, Berlin, Heidelberg, 1980. URL: <http://link.springer.com/10.1007/3-540-10000-8>. doi:10.1007/3-540-10000-8.
- [27] P. M. Suquet, Elements of Homogenization for Inelastic Solid Mechanics, in: E. Sanchez-Palencia, A. Zaoui (Eds.), *Homogenization Techniques for Composite Media*, Springer Nature, 1987, pp. 193–278.
- [28] M. Quintard, S. Whitaker, Transport in ordered and disordered porous media: volume-averaged equations, closure problems, and comparison with experiment, *Chemical Engineering Science* 48 (1993) 2537–2564.
- [29] Y. Davit, C. G. Bell, H. M. Byrne, L. A. Chapman, L. S. Kimpton, G. E. Lang, K. H. Leonard, J. M. Oliver, N. C. Pearson, R. J. Shipley, S. L. Waters, J. P. Whiteley, B. D. Wood, M. Quintard, Homogenization via formal multiscale asymptotics and volume averaging: How do the two techniques compare?, *Advances in Water Resources* 62 (2013) 178–206.
- [30] A. Wiegmann, A. Zemitis, EJ-HEAT: A Fast Explicit Jump Harmonic Averaging Solver for the Effective Heat Conductivity of Composite Materials, *Berichte des Fraunhofer ITWM* 94 (2006).
- [31] D. Baillis, R. Coquard, Radiative and Conductive Thermal Properties of Foams, in: *Cellular and Porous Materials: Thermal Properties Simulation and Prediction*, 2008, pp. 343–384. doi:10.1002/9783527621408.ch11.
- [32] ISO 8302:1991, Thermal insulation – Determination of steady-state thermal resistance and related properties – Guarded hot plate apparatus, International Organization for Standardization, 1991.
- [33] J. Schindelin, I. Arganda-Carreras, E. Frise, V. Kaynig, M. Longair, T. Pietzsch, S. Preibisch, C. Rueden, S. Saalfeld, B. Schmid, J.-Y. Tinevez, D. J. White, V. Hartenstein, K. Eliceiri, P. Tomancak, A. Cardona, Fiji: an open-source platform for biological-image analysis, *Nature Methods* 9 (2012) 676–682.
- [34] E. Brun, J. Vicente, F. Topin, R. Occelli, iMorph: A 3D morphological tool to fully analyse all kind of cellular materials, *Proceedings of the International Symposium on Cellular Metals for Structural and Functional Applications (CELLMET)* (2008) 1–6.
- [35] J. Randrianalisoa, D. Baillis, Thermal conductive and radiative properties of solid foams: Traditional and recent advanced modelling approaches, *Comptes Rendus Physique* 15 (2014) 683–695.
- [36] W. Y. Jang, A. M. Kraynik, S. Kyriakides, On the microstructure of open-cell foams and its effect on elastic properties, *International Journal of Solids and Structures* 45 (2008) 1845–1875.
- [37] P. Sepulveda, W. N. dos Santos, V. C. Pandolfelli, J. C. Bressiani, R. Taylor, *Thermal Conductivity of Gelcast Porous Alumina*, The American Ceramic Society Bulletin (1999).
- [38] N. J. Dyck, A. G. Straatman, A new approach to digital generation of spherical void phase porous media microstructures, *International Journal of Heat and Mass Transfer* 81 (2015) 470–477.
- [39] L. Onsager, Reciprocal Relations in Irreversible Processes. I, *Physical Review* 37 (1931) 405.
- [40] J. M. Powers, On the necessity of positive semi-definite conductivity and onsager reciprocity in modeling heat conduction in anisotropic media, *Journal of Heat Transfer* 126 (2004) 670–675.
- [41] S. Li, On the nature of periodic traction boundary conditions in micromechanical FE analyses of unit cells, *IMA Journal of Applied Mathematics (Institute of Mathematics and Its Applications)* 77 (2011) 441–450.
- [42] S. Hazanov, C. Huet, Order relationships for boundary conditions effect in heterogeneous bodies smaller than the representative volume, *Journal of the Mechanics and Physics of Solids* 42 (1994) 1995–2011.
- [43] D. S. Smith, S. Fayette, S. Grandjean, C. Martin, Thermal resistance of grain boundaries in alumina ceramics and refractories, *American Ceramic Society* 11 (2003) 105–111.
- [44] R. Coquard, D. Baillis, Modeling of Heat Transfer in Low-Density EPS Foams, *Journal of Heat Transfer* 128 (2006) 538.
- [45] Dassault Systèmes Simulia Corp., *Abaqus Analysis User’s Guide*, in: *Abaqus 2017 Documentation Collection*, 2017.
- [46] E. Mitsoulis, J. Vlachopoulos, The finite element method for flow and heat transfer analysis, *Advances in*

Polymer Technology 4 (1984) 107–121.

- [47] G. E. Archie, The Electrical Resistivity Log as an Aid in Determining Some Reservoir Characteristics, *Petroleum Technology* (1942) 54–62.
- [48] H. Moulinec, P. Suquet, A numerical method for computing the overall response of nonlinear composites with complex microstructure, *Computer Methods in Applied Mechanics and Engineering* 157 (1998) 69–94.
- [49] S. Brisard, K. Sab, L. Dormieux, New boundary conditions for the computation of the apparent stiffness of statistical volume elements, *Journal of the Mechanics and Physics of Solids* 61 (2013) 2638–2658.
- [50] M. Ostoja-Starzewski, S. Kale, P. Karimi, A. Malyarenko, B. Raghavan, S. I. Ranganathan, J. Zhang, Scaling to RVE in Random Media, in: *Advances in Applied Mechanics*, 1 ed., Elsevier Inc., 2016, pp. 111–211. URL: <http://dx.doi.org/10.1016/bs.aams.2016.07.001>. doi:10.1016/bs.aams.2016.07.001.